Response and Impact of Equatorial Ocean Dynamics and Tropical Instability Waves in the Tropical Atlantic under Global Warming: A regional coupled downscaling study

Hyodae Seo[1,2] and Shang-Ping Xie[1]

[1] International Pacific Research Center, SOEST, University of Hawaii, Manoa

[2] Physical Oceanography Department, Woods Hole Oceanographic Institution

Corresponding Author and Address:

Hyodae Seo, 266 Woods Hole Road, MS#21, Woods Hole, MA 02543

Email: hseo@whoi.edu, Tel: 508-289-2792

Submitted to *Journal of Geophysical Research –Oceans*

Revised on 24 November 2010

Abstract

A regional coupled model is used for a dynamic downscaling over the tropical Atlantic based on a global warming simulation carried out with the Geophysical Fluid Dynamics Laboratory CM2.1. The regional coupled model features a realistic representation of equatorial ocean dynamical processes such as the Tropical Instability Waves (TIWs) that are not adequately simulated in many global coupled climate models. The coupled downscaling hence provides a unique opportunity to assess their response and impact in a changing climate. Under global warming, both global and regional models exhibit an increased (decreased) rainfall in the tropical Northeast (South) Atlantic. Given this asymmetric change in mean state, the regional model produces the intensified near-surface cross-equatorial southerly wind and zonal currents. The equatorial cold tongue exhibits a reduced surface warming due to the enhanced upwelling. It is mainly associated with the increased vertical velocities driven by cross-equatorial wind, in contrast to the equatorial Pacific, where thermal stratification is suggested to be more important under global warming. The strengthened upwelling and zonal currents in turn amplify the dynamic instability of the equatorial ocean, thereby intensifying TIWs. The increased eddy heat flux significantly warms the equator and counter the effect of enhanced upwelling. Zonal eddy heat flux makes the largest contribution, suggesting a need for sustained monitoring of TIWs with spatially denser observational arrays in the equatorial oceans. Overall, results suggest that eddy heat flux is an important factor that may impact the mean state warming of equatorial oceans, as it does in the current climate.

1. Introduction

The equatorial Atlantic variability is dominated by an intrinsic mode of coupled variability akin to the El Niño-Southern Oscillation (ENSO) in the tropical Pacific Ocean [Zebiak, 1993] with a pronounced meridional mode on interannual timescales [*Carton et al.*, 1996; *Ruiz-Barradas et al.*, 2000; *Xie and Carton*, 2004]. The tropical Atlantic variability influences the variability of the intertropical convergence zone (ITCZ) and hence rainfall in the neighboring continents, particularly, in the regions of Northeastern Brazil [*Moura and Shukla*, 1981; *Hasternrath and Greischar*, 1993], the Sahel and coastal regions of Gulf of Guinea [*Giannini et al.*, 2003; *Chang et al.*, 2006]. It is also known to influence climate variability in other regions through interaction with the extratropics [e.g., *Okumura and Xie*, 2001; *Sutton et al.*, 2001]. Despite the climatic importance, it is still unclear how the equatorial Atlantic variability will respond to the increased anthropogenic greenhouse gas concentrations in a changing climate [e.g., *Breugem et al.*, 2007]. This is the focus of our study with an emphasis on the role played by dynamical processes and mesoscale eddies in the upper ocean.

Like the Pacific, the equatorial Atlantic ocean's response to global warming relies heavily upon ocean dynamical processes and heat transport that generate the non-uniform warming pattern in the upper ocean in spite of the uniform radiative heating [*Xie et al.*, 2010]. Models adopted so far for climate projection omit some potentially important ocean processes. One example is tropical instability waves (TIWs). They are generated from instabilities of equatorial zonal currents and fronts [e.g., *Philander*, 1976; *Cox*, 1980; *Yu et al.*, 1995; *Masina et al.*, 1999], common to both the tropical Atlantic [*Düing et al.*, 1975] and Pacific [*Legeckis*, 1977; *Legeckis et al.*, 1983]. Observations reveal TIWs as westward propagating wave-like oscillations of sea surface temperature (SST), ocean color [*Yoder et al.*, 1994], upper-ocean vortex [*Flament et al.*, 1996; *Kennan and Flament*, 2000], surface wind [*Chelton et al.*, 2001], and other properties near the equator with a typical wavelength of ~10° longitude and a phase speed of ~0.5 m s^{-1} [e.g., *Weisberg and Weingartner*, 1988; *Qiao and Weisberg*, 1995; *Chelton et al.*, 2000]. Being active during the upwelling season, TIWs are recognized as key organizers in heat, salt and momentum fluxes in the equatorial oceans [*Weisberg*, 1984; *Hansen and Paul*, 1984; *Bryden and Brady*, 1989; *Baturin and Niiler*, 1997]. In particular, TIWs affect the lower troposphere including wind and cloud distribution [*Hayes et al.*, 1989; *Wallace et al.*, 1989; *Deser et al.*, 1993; *Liu et al.*, 2000; *Hashizume et al.*, 2002; *Wu and Bowman*, 2007], inducing mesoscale air-sea interaction [*Chelton et al.*, 2005; *Seo et al.*, 2007b; *Small et al.*, 2008; *Small et al.*, 2009] and modulation of interannual variability in precipitation and wind in the tropics [*Jochum et al*., 2007]. They are typically characterized by subdaily time-scale adjustment processes and intense upper-ocean mixing [*Lien et al*., 2008; *Moum et al*., 2009], with cascades to larger scales [*Seo et al.*, 2006; *An*, 2008; *Nagura et al.*, 2008; *Zhang and Busalacchi*, 2008].

Considering the multi-scales and the air-sea interactions involved in TIWs, explicitly resolving them in the coupled climate models is important for simulation and prediction of tropical climate [e.g., *Jochum et al.*, 2008; *Roberts et al.*, 2009; *Shaffrey et al.*, 2009; *Ham and Kang*, 2010]. Most Intergovernmental Panel on Climate Change (IPCC)-class models, however, do not produce TIWs, hence their potential impacts have been left unexplored in the current discussion of tropical oceans' response to global warming.

To improve the projection of regional response to greenhouse forcing in the presence of complex feedbacks, climate models need to reduce their biases in mean state and should include a fuller spectrum of ocean-atmospheric processes such as TIWs as the mean state is important [*Fedorov and Philander*, 2001; *Wittenberg*, 2002; *Dewitte et al.*, 2007]. While the coupled general circulation models (CGCMs) are rapidly improving in these aspects [e.g., *Shaffrey et al.*, 2009], there is an alternative approach at present by downscaling such CGCM climate projections with high-resolution regional coupled models. The current study uses the Scripps Coupled Ocean-Atmosphere Regional (SCOAR) model [*Seo et al.*, 2007a] to perform, for the first time, a coupled dynamic downscaling experiment of an ensemble climate change projection carried out by the Geophysical Fluid Dynamics Laboratory (GFDL) CM2.1. Note that global climate models still produce large errors in representation of the mean states, and many features tend to be more deficient in the tropical Atlantic than the tropical Pacific [*Mechoso et al.*, 1995; *Davey et al.*, 2002]. *Richter and Xie* [2008] showed that, CM2.1 is not an exception, but tends to produce a relatively better mean state climatology than other models that participated in the IPCC Fourth Assessment Report (AR4). With a more accurate representation of oceanic processes, local air-sea coupling, and smaller biases by using a regional model [*Seo et al.*, *2006*; *Xie et al.*, 2007; *de Szoeke and Xie*, 2008], it is our goal to examine the adjustments of equatorial ocean processes under greenhouse gas forcing and assess their impact on ocean warming. We will mainly appeal to the current understanding of TIW effects on large-scale climate variability and tropical ocean response to global warming. Therefore, results presented in this study should be regarded rather experimental than conclusive. Coordinated regional coupled downscaling efforts for climate change projections will help gain an estimate of the robustness of regional projections based on multiple downscaling models.

The paper is organized as follows. Section 2 introduces the global and regional models, the experimental design and the data used for verification. Section 3 compares the downscaled climatology with observations, showing that key aspects of equatorial Atlantic climate, including the equatorial cold tongue and equatorial currents, are well captured in SCOAR. Section 4 investigates the change in mean state under global warming in SCOAR and CM2.1, which is important for the change in TIWs. Large-scale features such as the precipitation response in SCOAR are akin to those in CM2.1, indicating that lateral boundary conditions from CM.2.1 provide a reasonable constraint in atmospheric circulation in the regional coupled model. Important differences between SCOAR and CM2.1 arise in the equatorial regions, where air-sea coupling and oceanic internal variability are strong [*Jochum et al.,* 2004b]. Section 5 shows an increased variability of TIWs as a result of such changes in mean state. The net eddy temperature advection is a major element that determines the mixed layer heat budget under global warming. Section 6 is a summary and discusses implications for the debate on tropical ocean response to global warming.

2. Models and experiment

2.1 Global Coupled Model

The global coupled model that provides large-scale ocean and atmospheric fields is the GFDL CM2.1. It consists of GFDL atmospheric model (AM2.1) and the Modular Ocean Model version 4 (MOM4). AM2.1 uses 2.5° horizontal grid with 24 vertical levels and MOM4 uses the 1° horizontal resolution that increases to 1/3° towards the equator with 50 vertical levels. Details of the model formulation can be found in *Delworth et al.* [2006] and *Wittenberg et al.* [2006]. Note that the version of GFDL CM2.1 used in this study does not produce TIWs [*Wittenberg et al.*, 2006]. A 10-member ensemble-averaged simulation has been performed by GFDL for the A1B emission scenario up to 2050, and the monthly climatology fields of the atmosphere and oceanic variables for the period of 1996-2000 and 2046-2050 were provided to us to downscale. Since we have only monthly fields, it is not possible to directly downscale CM2.1. Hence we first compute the monthly differences between 1996-2000 for the 20th century (20C) climate and 2046-2050 for the A1B condition (A1B) to represent the mean warming signal (A1B-20C), and add it to the analysis products to downscale. Robustness of the warming pattern in CM2.1 from the 5-year ensemble mean (2046-2050) has been studied by Xie et al. [2010] in comparison to a simple model based on the gross moist instability and other CGCMs results (e.g., Vecchi and Soden [2007]). The ensemble averaging reduces internal variability and thus the difference in two penta-decades can be identified as response to greenhouse forcing.

2.2 Regional Coupled Model

Regional coupled model used to downscale the GFDL global fields is the Scripps Coupled Ocean-Atmosphere Regional (SCOAR) model [*Seo et al.*, 2007a]. The atmospheric component of SCOAR is the Regional Spectral Model (RSM, Juang and Kanamitsu [1994]), which is the downscaled version of the Global Spectral Model used in the NCEP Reanalysis 2 (NCEP2, *Kanamitsu et al.* [2002]) procedure. Downscaling allows the deterministic low-wavenumber and lateral boundary condition forcings of the regional domain that has dynamics consistent with the NCEP2 for the chosen period. The oceanic component is the Regional Ocean Modeling System (ROMS, *Haidvogel et al.* [2000] and *Shchepetkin and McWilliams*, [2005]), which is a state-of-the-art, free-surface hydrostatic primitive equation ocean circulation model with terrain-following, vertically stretched grids. These RSM and ROMS are coupled at daily frequency via bulk formula for wind stress and heat flux [*Fairall et al.*, 1996]. More details can be found by *Seo et al.* [2007a]. SCOAR has been previously used to examine TIWs and various aspects of the mean climate of the tropical Atlantic [*Seo et al.*, 2006, 2007b, 2008]. For this study, RSM uses ½° horizontal resolution with 28 levels and ROMS uses ¼° resolution with 30 sigma layers, which can capture the ocean mesoscale processes of interest [*Seo et al.*, 2007b]. Since TIWs are associated with a large zonal advective process [*Jochum and Murtugudde*, 2006], a denser zonal resolution is important in capturing the change in TIW characteristics, and ¼° zonal resolution in the regional model is more appropriate than 1° in CM2.1. The model domain covers the entire tropical Atlantic sector (30°S-30°N, 74°W-20°E), but this study focuses on the equatorial Atlantic Ocean (See Figure 2 for part of the model domain).

In the control (CTL) simulation, RSM downscales the 6-hourly NCEP2 for the atmosphere and the Simple Ocean Data Assimilation (SODA) monthly analysis [*Carton et al*., 2000] for the ocean as lateral boundary conditions for ROMS. The initial condition for ROMS in SCOAR is obtained from 50-year spin-up simulation forced by climatological atmospheric forcing and boundary conditions from SODA. RSM is initialized from January 1st 1980 00Z using NCEP2. The CO_2 concentration is set to 348 PPM and CH_4 and N_2O are fixed to the present-day values. The sea surface salinity (SSS) is restored to SODA monthly SSS fields because of river discharges into the tropical Atlantic (e.g., from the Congo and the Amazon Rivers) are not included. With this setup, CTL run is performed for 28 years from 1980 to 2007, the period when both the NCEP2 and SODA are available.

For the global warming (GW) simulation, we first compute the global warming signal by subtracting monthly fields of CM2.1 20C (1996-2000) from CM2.1 A1B (2046-2050). In the atmosphere, monthly differences in temperature, u-, v- velocities and relative humidity at each pressure level are interpolated to 6-hour intervals and added to the NCEP2. These pressure level fields are then converted to sigma level using NCEP2 surface pressure by the method described by *Yoshimura and Kanamitsu* [2009]. Hence the method assumes that the impact of atmospheric internal variability from the boundary conditions contained in NCEP2 is identical between two runs. In the ocean, monthly difference in temperature and salinity are added to monthly SODA analysis. Now that we are modifying the seasonal cycle only, the global warming forcing in the current experimental setup has a minimal impact on the interannual cold tongue variability (not shown), but produce a significant change in seasonal cycle (Section 4.1). CO_2 concentration in GW run is increased to 521.75 PPM, representing an about 50% increase from the CTL run consistent with the background field. Other greenhouse gases are held to the present-day value. Since the temperature and large-scale circulation fields already contain the effect of elevated level of greenhouse gas concentrations, this will not change the conclusion of the results; but it may underestimate the warming amplitude in the regional model [*M. Kanamitsu, pers. comm*.; Section 4.1]. SSS in GW is restored to SODA monthly SSS plus differences inferred from 20C and A1B in CM2.1. With an identical setup otherwise, GW run is also performed for the same period of time.

Adding global warming anomalies to the observed mean state is essentially the same in spirit as an anomaly nesting method used for seasonal prediction [e.g., *Vasubandhu and Kanamitsu*, 2004]. In the global warming literature, it is often referred to as a pseudo global warming method [e.g., *Kimura and Kitoh*, 2007; *Knutson et al.*, 2008; *Kawase et al.*, 2009, Zahn and von Storch, 2010]. An obvious advantage is to sidestep mean state errors in global models, a problem that is particularly severe in the tropical Atlantic sector. However, the method does not consider changes in submonthly disturbances of low wavenumbers under global warming, as it needs the reanalyses as background forcing. Note that TIWs are of high wavenumbers that are not constrained by high wavenumber forcing in the reanalysis boundary conditions. Hence, in order to highlight the importance of the missing TIWs in the global models, we explore the their effect in the regional model by downscaling the low wavenumber response under global warming. Uncertainty due to change in high-frequency oceanic variability and the atmospheric internal variability in boundary conditions will be explored in future studies.

It should be also noted that the length of the downscaling simulation is limited to the period of the available background flows (i.e., 28-years of NCEP2 and SODA), which may be not long enough for the coupled system to reach a new steady state, particularly in the ocean. Figure 1 shows the evolution of the annual mean temperature difference (GW-CTL) averaged over the cold tongue region (1°S-1°N, 30°W-10°W). The surface intensified warming signal slowly propagates downward after the initialization. Being far from the lateral boundaries, it takes roughly 20 years before the upper equatorial warming trend exhibits a quasi-steady evolution. For the thermocline, the equilibrium may take more than several decades [e.g., *Liu*, 1998]. The analyses presented here are based on the period of the final 10-years (1998-2007), which is close to a quasi-steady state for the upper thermocline. This is perhaps appropriate because the A1B projection itself is not in full equilibrium in 2046-2050. A different choice of period (e.g., 20 years), however, does not change the results discussed below.

2.3 Observational Data

The observed SST data are obtained from the daily NOAA Optimum Interpolation (NOAA OI) SST Analysis version 2 on a 0.25° grid [*Reynolds et al.*, 2007] and the observed rainfall is from the monthly Tropical Rainfall Measuring Mission (TRMM) precipitation product 3B43 Version 6 [*Huffman et al.*, 2007] that combines the TRMM data with an estimate from the global gridded rain gauge data on a 0.25° grid, both from the period of 1998-2007. The 10-m winds are obtained from NCEP2 for the same period. The observed net surface heat flux is obtained from the estimate from the global Objectively Analyzed Air-Sea Fluxes [*Yu and Weller*, 2007] from the period of 1998-2004. These observations are interpolated to model's horizontal grid.

3. Present-day climate simulation

This section examines the simulation on the annual mean and seasonal cycle of equatorial Atlantic climate from SCOAR (CTL) in comparison to observations (OBS) and CM2.1 (20C). In observations (Figure 2a), the annual mean equatorial Atlantic shows a zonal gradient in SST with warm west and cold east. Annual mean winds are cross-equatorial with an easterly component on the equator, which is important for the development and maintenance of this east-east contrast. In CM2.1, as in many CGCMs [*Richter and Xie*, 2008], this east-west gradient is reversed, with the cold tongue too weak and shifted to the western equatorial Atlantic (Figure 2c). The SCOAR CTL displays a strong cold tongue at the central/eastern equatorial Atlantic. A stronger cold tongue in SCOAR appears to be associated with stronger easterly winds at the equator than in CM2.1 and observations. The maximum net heat flux (contours in Figure 2b,d,f) is into the ocean over the cold tongue, both in the observations and the models. It is noteworthy that SCOAR produces generally colder SSTs and underestimates the rainfall amount throughout the domain compared to the observations. It is perhaps due to the underestimation of the net heat flux into the ocean as seen in Figures 2 associated with the errors in cloudiness and shortwave radiation flux. The strong winds in SCOAR could have also contributed to strong mixing and evaporation.

Figure 3 shows the simulated annual mean zonal equatorial currents. Both in the zonal and meridional transects, the Equatorial Undercurrent (EUC) in SCOAR is found at the depth of 75 meters with a narrow meridional scale and the speed exceeding 80 cm/s, features that are similar to SODA as well as the estimates derived from the in situ measurement [e.g., *Schott et al.*, 2003; *Brandt et al.*, 2006]. Both the observed northern and southern branches of the South Equatorial Current (SEC) at the surface are also well captured in the downscaled model (Figure 3b). CM2.1 generally underestimates the amplitudes of EUC and SEC, with much broader scales of EUC core and no distinction of two branches of SEC. Overall, downscaling produces a quite realistic simulation of equatorial currents and the cold tongue structure, which is a critical requirement for studying dynamic instability and energetics of the equatorial ocean as discussed in Sections 4 and 5.

The annual mean SST in SCOAR is generally colder than observations throughout the domain, which may be responsible for the underestimation of precipitation in the marine ITCZ (Figure 2f). Generally, SCOAR and CM2.1 share similar spatial patterns of annual rainfall climatology, including a hint of the secondary ITCZ south of the equator. This indicates that the downscaled large-scale atmospheric circulation, unlike the oceanic features that are distinct from those of global model, is largely determined by the boundary conditions.

The top panel of Figure 4 shows the annual cycle of equatorial SST as a function of longitude and calendar month. CM2.1 underestimates the cold tongue temperature during the upwelling season and overestimates it during the boreal spring. The SCOAR captures realistic cold tongue temperature and its evolution, although the boreal spring SST is too cold. The amplitudes of the equatorial annual cycle (Figure 4f) are somewhat overestimated in CM2.1 (solid blue line) [*Breugem et al.*, 2006] and underestimated in SCOAR (shaded blue line).

4. Global warming response

In order to examine the change in TIWs under global warming, one needs to consider the change in large-scale annual mean state first, as this change drives the adjustment in equatorial ocean variability and, in particular, TIWs.

4.1 Annual mean and seasonal cycle

Under global warming, the annual mean changes in both CM2.1 (A1B-20C) and SCOAR (GW-CTL) show a basin-wide warming pattern (Figures 5a,c). Generally, SCOAR exhibits smaller warming in surface temperature than CM2.1 partly due to the fixed concentration of greenhouse gases other than CO_2 in the GW run and the stronger wind speed. Note that, despite the basin-wide warming, there are important spatial patterns both in the global and regional models. For example, there is a reduced warming near the equator and the coasts where ocean dynamics likely play a role in modulating SSTs. The reduced warming pattern is more pronounced in the regional model, due to a more accurate representation of such ocean dynamical processes as upwelling (Section 4.2).

In the equatorial Atlantic west of 30°W, both SCOAR and CM2.1 show that the change in net surface heat flux is weakly negative (cooling the ocean). The negative net surface heat flux in this region is dominated by a reduction of shortwave radiation and increased cloudiness (Figure 6), suggesting that the increased convective clouds are partially responsible for the reduced warming in the western equatorial ocean. In the central and eastern Atlantic (30-10°W), the change in net surface heat flux is positive in CM2.1 (Figure 5b), where the enhanced equatorial upwelling balances the increase in surface heat flux into the ocean [*Xie et al.*, 2010]. On the other hand, SCOAR features a weak negative heat flux change. This different pattern of surface heat flux change is due to the oceanic heat flux by TIWs that are energized in SCOAR, adding heat to the cold tongue, an important feature that is not resolved in CM2.1 (Sections 4.3 and 5).

Rainfall generally increases (decreases) in the tropical Northeast (South) Atlantic (Figure 5d,b). This large-scale asymmetric convective response would drive the cross-equatorial southerly flows [*Lindzen and Nigam*, 1987]. Note that the regional model produces a stronger response in this near-surface cross-equatorial meridional wind than the global model because of its stronger coupling to the equatorial SST of the regional model. This acceleration of the cross-equatorial wind would further enhance the magnitude of asymmetric change in atmospheric convection in the regional model (Figure 5d). The increase in cross-equatorial near-surface southerly wind has important consequences to the changes in vertical motions on the equator, as is further discussed in Section 4.3.

The change in the annual cycle of cold tongue SST in CM2.1 is characterized by two peaks in reduced warming in boreal spring (March) and boreal fall (August) (Figure 4d). A strengthening of the equatorial southeasterlies during the boreal spring in CM2.1 A1B appears to correspond to the reduced warming there, while little change in wind during the boreal fall suggests that enhanced oceanic vertical heat transport is locally responsible for the reduced warming over the cold tongue. Note also the cross-equatorial wind anomaly in advance of this reduced warming of SSTs during the cold season, suggesting the importance of meridional winds for the equatorial annual cycle [*Mitchell and Wallace*, 1992; *Xie*, 1994; *Chang*, 1994]. In SCOAR, the reduction in SST warming takes place from March to October (Figure 4e), associated with the intensified southeasterlies followed by the southerly wind anomalies.

4.2 Why is there a reduced warming over the equatorial cold tongue?

An important ocean process for SST in the equatorial cold tongue is the vertical advection of temperature (upwelling). Vertical mixing (diffusion) also changes in the model, but its magnitude is smaller than vertical temperature advection (see black curve in Figure 11b). Change in horizontal temperature advection is discussed using a full three-dimensional heat budget analysis in Section 5. The vertical temperature advection, $-wT_z$, under global warming can be simply decomposed into the four terms as follows:

$$-wT_z = -\langle w\rangle\langle T_z\rangle - \langle w\rangle T_z^* - w^*\langle T\rangle_z - w^*T_z^*, \qquad (1)$$

where the temperature (T) and vertical velocity (w) are decomposed into the present-day condition ($\langle\ \rangle$) and the global warming perturbation (*, GW-CTL). The subscripts denote partial derivatives. The first term on the right hand side is the climatological upwelling in CTL, and the second term denotes the advection due to the climatological vertical velocities acting on the anomalous temperature gradient, representing an ocean dynamical thermostat mechanism proposed in the equatorial Pacific [*Clement et al.*, 1996; *Cane et al.*, 1997]. The third term denotes the advection due to the anomalous vertical velocities acting on the climatological temperature gradient. The last term is negligible. Figure 7 compares the annual mean magnitudes of the first three terms of (1). Climatological upwelling is the largest cooling term throughout the equatorial Atlantic as expected (Figure 7a). The second term in Figure 7b shows a weak warming (cooling) in the western (eastern) equatorial Atlantic. The weak warming in the west (40-20°W) is due to the reversed vertical temperature gradient in the upper ocean (dT^*/dz) associated with the reduced surface warming in response to a decrease in shortwave radiation flux (Figure 6a), while the weak cooling in the eastern equatorial Atlantic (20-0°W) is due to the strengthened vertical temperature gradient associated with the surface-intensified warming. Overall the second term is smaller than the third (Figure 7c), which features strong cooling in the thermocline because of the increase in upwelling velocity (w^*) associated with the divergence of the surface wind and current anomalies [*Chang et al.*, 2006]. The effect of increased w^* in the third term dominates, leading to the reduced surface warming in the cold tongue.

DiNezio et al. [2009] showed in the Pacific that the enhanced vertical temperature advection, the second term in (1), is largely due to the strengthened thermal stratification (dT^*/dz, *Clement et al.* [1996]). This is in contrast to the Atlantic where local surface divergence in wind due to the intensified cross-equatorial southerly increases the advection of mean vertical temperature gradient by the anomalous upwelling (w^*). This difference is closely related to the distinct equatorial processes between the Pacific and Atlantic [*Chang et al.*, 2006]. In the Pacific, low-frequency variability of SST in the cold tongue is largely due to the basin-scale thermocline adjustment that connects the western Pacific warm pool to the eastern Pacific cold tongue through equatorial ocean dynamics that sustains this contrast. In the Atlantic, on the other hand, mainly due to the narrow zonal width, local wind-induced upwelling plays a more important role [*Zebiak*, 1993; *Carton and Zhou*, 1997].

4.3 Changes in ocean currents, dynamic instability and TIWs

Figure 8 shows the zonal and meridional transects of the changes in zonal currents (shades) with the present-day climatology superposed (contours) as in Figure 3. Both CM2.1 and SCOAR tend to suggest a spin-up of the SEC and EUC, largely driven by change in winds, but SCOAR shows a much greater strengthening of currents. The increased SEC and EUC can be viewed as a nonlinear response of the equatorial zonal currents to the intensified cross-equatorial southerlies. Consider an idealized solution by *Philander and Delecluse* [1983] where the zonal flows are forced by cross-equatorial meridional wind. The linear response of the ocean to this cross-equatorial southerly is to generate the northward (southward) surface (subsurface) currents, with the downwelling (upwelling) at 3°N (3°S), forming a closed meridional circulation. The southerly wind also introduces zonal currents through Ekman drift, generating westward (eastward) surface current in the south (north) of the equator with weak opposite flows below the surface, where winds are of secondary impact and the Coriolis force causes a weak equatorial current at right angles to the southward pressure force. When the effect of nonlinear advection is taken into account, the surface meridional current advects the westward surface momentum from the south to the north of the equator, hence generating stronger westward flows in the north. This is accompanied by a large meridional shear of the zonal currents at 3°N, indicative of the increased meridional shear between SEC and North Equatorial Counter Current (NECC). A weak eastward subsurface current develops into a strong eastward jet in the south of equator, which shifts the center of the EUC slightly southward and strengthens the EUC (see also *Yu et al.* [1997]). The response to idealized wind forcing is similar to what is illustrated in Figures 8a and 9. The greater increase in SCOAR currents is due to greater anomalies in cross-equatorial wind associated with the change in large-scale atmospheric circulation. It is also possible that a strong TIW variability in SCOAR strengthens the SEC and EUC through the vorticity flux convergence, a positive feedback via eddy-mean flow interaction [*Kug et al.*, 2010]. CM2.1 lacks this positive feedback without TIWs, leading to a weak low-frequency zonal current on the equator.

The strengthening of SEC/EUC and the increased shear in SEC/NECC by the meridional wind affects dynamical instabilities that energize TIWs. Figure 9 shows the two main sources of eddy kinetic energy (EKE): the barotropic conversion, $-\rho_o \vec{u'} \cdot (\vec{u'} \cdot \vec{\nabla}\vec{U})$ and the baroclinic conversion, $-g\rho' w'$, where ρ is the density, primes denote eddy variability and U is the mean zonal current [*Masina et al.*, 1999; *Jochum et al.*, 2004a]. These EKE source terms increase significantly under global warming in SCOAR. Two peaks in barotropic conversion at 0.5°N and 3°N correspond to the regions of maximum shear in EUC/SEC and SEC/NECC. Both increase in GW, contributing to increased amplitude of $-\rho_0 u'v'U_y$. Also the increased vertical shear between SEC and EUC and the strengthened SST front substantially elevate the baroclinc conversion in a broad region north of the equator [*von Schuckmann et al.*, 2008].

The increase in these two types of energy source terms in the EKE equation leads to the intensified variability of TIWs. Figures 10a,b (Figures 10c,d) show the maps of EKE (SST variance) defined as $EKE = ½(u'^2 + v'^2)$, where the prime denotes a 20-40 day band-pass filtered field. Over the region where TIWs are energetic, both these dynamic and thermodynamic measures of TIWs are enhanced by 31% and 36 % respectively during JJA. In the annual cycle of EKE and SST variance (Figures 10e,f), it is during the upwelling season that eddy variability is most enhanced (May-September), when the cross-equatorial winds are strong and cold tongue variability is tightly coupled to wind variability.

5. Upper ocean heat budget

TIWs significantly contribute to the heat budget of the equatorial ocean through eddy temperature advection. Therefore, strengthened TIWs variability may play an important role in the equatorial heat budget under global warming. This section diagnoses the change in eddy temperature advection by TIWs and assesses its contribution to the heat balance within the cold tongue.

The governing equation for mixed layer temperature in the advective form is

$$T_t = -\vec{u}_H \cdot \vec{\nabla}_H T - wT_z + \frac{Q}{\rho c_p H} + R \qquad (2)$$

where T is the temperature, $\vec{u}_H$ is the horizontal velocity vector and w the vertical velocity. $\vec{\nabla}_H$ is the horizontal gradient operator, Q the net surface heat flux (positive into the ocean), ρ the density of sea water, c_p its heat capacity and H the monthly varying mixed layer depth (MLD). The subscripts t and z denote partial derivatives in time and depth, respectively. Using an advective form, it is easier to separate the eddy part from the mean current without having to carry the variable mixed layer depth. Temperature tendency in (2) is determined by horizontal and vertical advections of temperature as well as the atmospheric heat flux into the ocean. The residual R includes entrainment, horizontal and vertical diffusion and other unresolved processes. Note that ROMS uses no explicit horizontal diffusion, but employs an implicit scale-selective smoothing in the third-order upstream biased advection scheme [*Haidvogel et al.*, 2000]. However, horizontal diffusion is small in the heat budget of the high-resolution model [*Jochum et al.*, 2005]. Other unresolved processes are likely to be non-negligible [*Wang and McPhaden*, 1999]. On the equator, R predominantly represents entrainment via vertical diffusion (not shown).

The horizontal and vertical advection terms in (2) can be further decomposed as,

$$-\vec{u}_H \cdot \vec{\nabla}_H T - wT_z = -\overline{uT_x} - \overline{vT_y} - \overline{wT_z} - u'T'_x - v'T'_y - w'T'_z, \qquad (3)$$

where over-bars denote the mean plus seasonal cycle (monthly averages) and the prime denotes the deviations representing TIW variability. The first two terms on the right hand side is the contribution of the mean horizontal advection to the heat budget and the third term is the mean vertical advection. This vertical advection, $-\overline{wT_z}$ in (3) and the entrainment via vertical diffusion (R) in (2) are not cleanly separable at the bottom of the mixed layer with varying depth [*Wang and McPhaden*, 1999; *Jochum and Murtugudde*, 2006]. For this reason, we combine $-\overline{wT_z}$ and R collectively as upwelling and entrainment.

The last three terms in (3) are contributions from TIWs. In particular, the last term, $-w'T_z'$, is the TIW-induced vertical mixing. Because the model does not save the vertical diffusion term at every model time-step, in principle it is not possible to distinguish vertical diffusion due to eddies from that due to the mean shear [*Schudlich and Price*, 1992; *Jochum and Murtugudde*, 2006; *Menkes et al.*, 2006]. However, since TIW-induced vertical mixing is known to be an important element that may offset horizontal eddy heat flux [*Jochum et al.*, 2004a; *Menkes et al.*, 2006; *Moum et al.*, 2009], it needs to be included in assessment of the TIW contribution to the equatorial heat budget.

Figure 11a shows the annual mean heat budget zonally averaged over the cold tongue (30°W-10°W), where the eddy activity is largest. In CTL (solid curves), the upwelling and entrainment (black curve) are symmetric about the equator with an equatorial peak. The mean horizontal advection (blue curve) is dominated by the poleward Ekman divergence, which is not very pronounced north of the equator because of the eastward turning of the wind vectors. Weak latent heat flux leads to a maximum in net atmospheric heat flux on the equator (red curve). TIWs significantly warm the equator by $-v'T_y'$ (Figure 12b) [e.g., *Hansen and Paul*, 1984]. TIW also warm the region from the equator to 2°N through $-u'T_x'$ (Figure 12a), which is comparable in magnitude to $-v'T_y'$. This sizable warming by TIW zonal advection is primarily due to the spatial patterns of anomalies in SST and current associated with the TIWs. This is demonstrated in Figure 13a (Figure 13b) with the total (spatially high-pass filtered) fields from the CTL simulation. SST anomalies are more meridionally stretched with narrower zonal width. As a result, T_x' tends to be greater than T_y'. Note also that there is an obvious correlation between the eastward SST gradient and westward currents in the anomaly fields, which leads to a stronger zonal advection of temperature by the anticyclonic vortices of the waves [*Jochum and Murtugudde*, 2006].

The net warming by eddy horizontal temperature advection tends to be offset by $-w'T_z'$ (Figure 12c). This cooling by $-w'T_z'$ occurs over the regions of strong shear due to TIW current anomalies, where the turbulent mixing/entrainment is large [*Kennan and Flament*, 2000; *Menkes et al.*, 2006; *Lien et al.*, 2008; Moum et al., 2009]. Furthermore, in the warm phase of TIWs, the perturbation wind speed increases [Figure 13c, *Liu et al.*, 2000; *Chelton et al*., 2001; *Hashizume et al.*, 2002], enhancing the mechanical energy for turbulent mixing at the center of TIW vortices having large vertical motion [*Menkes et al.*, 2006]. Overall, the total three-dimensional eddy temperature advection leads to a net warming of the equator (Figure 12d and magenta curve in Figure 11a).

Figure 11b show the GW-CTL changes in major components of the heat budget. In GW, equatorial upwelling increases slightly north of the equator (black curve), and so does the eddy temperature advection (magenta curve). One important difference is that the former is driven by the large-scale circulation that connects the increased meridional surface wind to equatorial upwelling velocities, while the latter is generated by downscaling and counteracts the net impact of the former. Indeed this increase in net eddy heat flux is the largest term that balances the cooling due to increased upwelling north of the equator. Advection by mean current changes also exerts a warming effect (blue curve in Figure 11c) while surface heat flux change (red curve in Figure 11c) is weakly negative due to the reduced shortwave radiation and heating by TIWs.

Table 1 summarizes the changes in heat budget terms for 10-year mean over 1°S-3°N. Also included are separate heat budget results for upwelling season (JJA) when TIWs develop and their effects are large. The annual mean increase in upwelling cools the equator by 0.05 °C month^{-1}, with an additional cooling of 0.05 °C month^{-1} by net negative heat flux. The combined cooling is opposed by the warming caused by mean horizontal advection (0.07 °C month^{-1}) and eddy heat flux by TIWs (0.03 °C month^{-1}). During the cold season, the warming by eddy advection substantially intensifies (0.12 °C month^{-1}), becoming the most important warming agent for the equatorial cold tongue.

As TIWs are energized under global warming, each element of the eddy temperature advection also strengthens. Note that the zonal advection shows the largest warming (red curve in Figure 11b and also Figure 12). This is primarily due to the aforementioned structure of the SST gradient and the current anomalies of TIWs in the present-day condition, which are both more strengthened under global warming due to the stronger front and the westward SEC. The stronger currents, shears, and SST anomalies associated with TIWs also increase the vertical temperature advection by TIWs, which tend to offset the warming effect by the horizontal eddy advection. Overall, the change in net eddy advection significantly warms the equatorial mixed layer with a peak displaced slightly to the north. Note also that it is this warming of cold tongue by TIWs that reduces the surface heat flux into the cold tongue in SCOAR (Figure 5d), while in CM2.1, without TIWs, the cooling effect by equatorial upwelling induces greater net surface heat flux anomalies into the ocean (Figure 5b).

6. Conclusions and Discussion

Response of equatorial SST to global warming is affected by a number of processes, such as equatorial upwelling [*Clement et al.*, 1996], subtropical-tropical interaction [*Seager and Murtugudde*, 1997; *Liu*, 1998; *Liu et al.*, 2005], a weakened Walker circulation and westerly wind-induced thermocline feedback [*Vecchi et al.*, 2006; *Vecchi and Soden*, 2007], temperature-evaporation feedback [*Knutson and Manabe*, 1995; *Liu et al.*, 2005; *Xie et al.*, 2010], and shortwave cloud forcing [*Graham and Barnett*, 1987; *Ramanathan and Collins*, 1991; *Klein and Hartman*, 1993; *Meehl and Washington*, 1996; *Miller* 1997, *Li et al.*, 2000; *Clement et al.*, 2009]. Understanding these processes and their adjustments is important as they shape the SST response pattern to global warming.

The main goal of this paper is to demonstrate that having TIWs in the equatorial oceans may bring advantage to the interpretation of warming patterns since they produce sizable eddy heat flux that interacts with these climate feedback processes. In order to better resolve TIWs, it is necessary to have the realistic equatorial wind and currents, the sharp thermocline, and the strong air-sea interactions, which are under-represented in the climate models with high ocean viscosity and coarse atmospheric resolution. In this study, we deliver a new regional coupled dynamical downscaling technique to the climate modeling community for assessing the regional aspects of global climate change. With better representation of the equatorial oceanic processes including explicitly resolving TIWs, the regional coupled models can provide a useful guidance to improving parameterization of the effect of TIWs in the GCMs and simulation of the equatorial climate thereof.

In this first coupled downscaling of climate change projections over the tropical Atlantic, SST warming is reduced on the equator owing to the vertical temperature advection. The increased ocean upwelling in the cold tongue is associated with the locally increased ocean vertical velocities on the equator (w^*, the third term in (1)), which are driven by the strengthening of the cross-equatorial surface winds. This is in contrast to the tropical eastern Pacific, where the increased vertical heat transport is largely due to the enhanced thermal stratification (dT^*/dz, the second term in (1), *DiNezio et al.* [2009]). The anomalous cross-equatorial surface wind intensifies the zonal currents [*Philander and Delecluse*, 1983; *Yu et al.*, 1997] that amplify the dynamic instability associated with the horizontal and vertical shear of these currents. Studies show that most of the EUC water upwells in the equatorial cold tongue, suggesting a negative correlation between EUC transport and the cold tongue temperature [*Hazeleger and de Vries*, 2003; *Hormann and Brandt*, 2007]. This is in line with the fact that CM2.1 is characterized by weak EUC and warm cold tongue, as opposed to the SCOAR with stronger EUC and colder cold tongue. The increased baroclinic and barotropic instability of the ocean intensifies EKE in the ocean and hence TIWs. The sizeable net eddy heat advection is important in the anomalous heat budget, acting to warm the equatorial ocean and counter the effect of enhanced upwelling. If TIWs were not part of the adjustment, the enhanced upwelling would lead to a greater reduction of SST warming on the equator, causing larger surface heat flux anomalies into the ocean, which is happening in CM2.1

The changes in mean state under global warming modify TIWs, which in turn feeds back to the upper ocean heat balance through eddy temperature advection. Zonal advection by TIWs dominates this change in eddy heat flux, suggesting a need for sustained monitoring of TIW variability with zonally dense observational arrays. TIW-induced entrainment tends to offset the increase in the zonal eddy heat flux, because the warmer SST and increased zonal SST gradients would lead to stronger turbulent mixing through the stronger fronts and turbulent mixing. Moreover, increased thermal stratification strengthens the upwelling effect on SST on the equator.

It has been well recognized that TIWs may act as natural iron fertilizers, as illustrated by the enhanced primary productivity in a “line in the sea” along the SST fronts of the TIWs [*Yoder et al.*, 1994]. TIWs strongly modulate plankton biomass and carbon export in the eastern Pacific through vertical turbulent mixing and horizontal advection [e.g., *Chavez et al.*, 1999; *Strutton et al.*, 2001; *Gorgues et al.*, 2005; *Evans et al.*, 2009]. In an eddy-permitting coupled physical-biological model, *Löptien et al.* [2009] have shown that biological feedbacks increase the vertical shear of the equatorial currents, thereby leading to a significant intensification of TIWs. It is yet to be examined whether and how the changes in external forcing under global warming interact with the ocean biology and contribute to the equatorial heat balance through TIWs and biological feedbacks, especially in relation to other complex feedbacks involved in forming SST warming response pattern.

The CGCMs that we use for projection of the future climate change still exhibit a wide range of errors in reproducing the observed present-day climate of the tropical Atlantic [Richter and Xie, 2008]. Downscaling such global model simulations improves some aspect of the climatic processes, as exemplified by the EUC, cold tongue, and TIW in this study. However, the large-scale circulation in the regional model is inevitably influenced by the boundary condition provided from such CGCMs. A thorough validation of the global model simulations with the multiple instrumental measurements is an essential step towards the robust assessment of the regional climate change in a regional coupled model. Alternatively, idealized experiments with the prescribed climate change forcing (such as the intensified inter-hemispheric winds discussed in this study) would allow an identification of the regional climate change signals without the issues due to such biases in global models.

Finally, TIWs are more energetic in the tropical Pacific with stronger mixing and eddy heat flux. They are intimately coupled to the mean state of the deep tropical Pacific and the evolution of ENSO [Yu and Liu, 2003], with the global impact on climate and weather [e.g., *Alexander et al.*, 2002]. Therefore, its potential impact on the mean and low-frequency variability of the tropical Pacific in a changing climate should be addressed in more detail by explicitly resolving them in a long-term climate simulation. It is our future goal to extend the current study into the equatorial Pacific Ocean based on the multiple CGCMs simulations from the upcoming IPCC Fifth Assessment Report (AR5) and the Coupled Model Intercomparison Project Phase 5 (CMIP5) in order to explore their role in climate on broader scales. The current study is the first attempt at the coupled dynamical downscaling of climate change projections. We hope that this exploratory research will stimulate more coordinated regional coupled downscaling efforts for climate change scenarios using the CMIP5 simulations to resolve spatial scales important for climate change projection and adaptation.

Acknowledgements

HS acknowledges the support from the NOAA Climate and Global Change Postdoctoral Fellowship Program and The Penzance Endowed Fund in Support of Assistant Scientists at WHOI. HS and SPX thank support from NOAA, NSF and the Japan Agency for Marine-Earth Science and Technology. The authors acknowledge the Center for Observations, Modeling and Prediction at Scripps (COMPAS) for providing the required computer resources for the SCOAR model simulation. The authors also thank the GFDL for providing the ensemble averaged model outputs. HS thanks the input of Yoshimura, Kanamitsu, Kim, Richter, and Lauer and comments by Murtugudde and Jochum. Authors thank the anonymous reviewers for their comments and suggestions, which substantially improved the manuscript. The NCEP Reanalysis 2 and NOAA OI SST data were provided by the NOAA/OAR/ESRL PSD, Boulder, Colorado, USA, from their web site at http://www.cdc.noaa.gov. The TRMM 3B43 V6 rainfall data are obtained from

http://disc.sci.gsfc.nasa.gov and WHOI OAFlux from http://oaflux.whoi.edu. The Asia-Pacific Data Research Center of the IPRC provided the monthly SODA analysis through its web site at http://apdrc.soest.hawaii.edu. IPRC/SOEST publication number #xxx/yyy.

References

Alexander M. A, I. Blade, M. Newman, J. R. Lanzante, N. Lau, J. Scott (2002), The atmospheric bridge: The influence of ENSO teleconnections on air-sea interaction over global oceans, *J. Climate, 15*, 2205 – 2231.

An, S. I. (2008), Interannual Variations of the Tropical Ocean Instability Wave and ENSO, *J. Climate, 21*, 3680–3686.

Baturin, N. G., P. P. Niiler (1997), Effects of instability waves in the mixed layer of the equatorial Pacific, *J. Geophys. Res., 102*, 27771-27794.

Baturin, N. G. and P. P. Niiler (1997), Effects of instability waves in the mixed layer of the equatorial Pacific, *J. Geophys. Res., 102*, 27771-27794.

Brandt P., F. A. Schott, C. Provost, A. Kartavtseff, V. Hormann, B. Bourles, and J. Fischer (2006), Circulation in the central equatorial Atlantic-mean and intraseasonal to seasonal variability, *Geophys. Res. Lett., 33*, L07609.

Breugem, W. P., W. Hazeleger, R. J. Haarsma (2006), Multimodel study of tropical Atlantic variability and change, *Geophys. Res. Lett., 33*, L23706.

Breugem, W. P., W. Hazeleger, and R. J. Haarsma (2007), Mechanisms of northern tropical Atlantic variability and response to CO2 doubling, *J. Climate*, *20*, 2691-2705.

Bryden, H. L., E. C. Brady (1989), Eddy momentum and heat fluxes and their effect on the circulation of the equatorial Pacific Ocean, *J. Mar. Res.*, *47*, 55-79.

Cane, M., A. C. Clement, A. Kaplan, Y. Kushnir, D. Pozdnyakov, R. Seager, S. E. Zebiak, R. Murtugudde (1997), Twentieth-century sea surface temperature trends, *Science, 275*, 957-960.

Carton, J. A., X. Cao, B. S. Giese, and A. M. da Silva (1996), Decadal and interannual SST variability in the tropical Atlantic Ocean, *J. Phys. Oceanogr., 26*, 1165-1175.

Carton, J. A., Z. Zhou (1997), Annual cycle of sea surface temperature in the tropical Atlantic Ocean, *J. Geophys. Res., 102*, 27813-27824.

Carton, J. A., G. Chepurin, X. Cao, B. Giese (2000), A simple ocean data assimilation analysis of the global upper ocean 1950 – 95. Part I: Methodology, *J. Phys. Oceanogr., 30,* 294 –309.

Chang, P. (1994), A study of the seasonal cycle of sea surface temperature in the tropical Pacific Ocean using reduced gravity models, *J. Geophys. Res., 99*, 7725–7741.

Chang. P., T. Yamagata, P. Schopf, S. K. Behera, J. Carton, W. S. Kessler, G. Meyers, T. Qu, F. Schott, S. Shetye, S.-P. Xie (2006) Climate Fluctuations of Tropical Coupled Systems—The Role of Ocean Dynamics, *J. Climate, 19*, 5122–5174.

Chavez, F. P., P. G. Strutton, G. E. Friedrich, R. A. Feely, G. Feldman, D. Folay, M. J. McPhaden (1999), Biological and chemical response of the equatorial Pacific Ocean to the 1997-98 El Niño, *Science, 286*, 2126-2131.

Chelton, D. B., F. J. Wentz, C. L. Gentemann, R. A. de Szoeke, M. G. Schlax (2000), Satellite Microwave SST Observations of Transequatorial Tropical Instability Waves, *Geophys. Res. Lett., 27*, 1239-1242.

Chelton, D. B., S. K. Esbensen, M. G. Schlax, N. Thum, M H. Freilich, F. J. Wentz, C. L. Gentemann, M. J. McPhaden, P. S. Schopf (2001), Observations of coupling between surface wind stress and sea surface temperature in the eastern tropical Pacific, *J. Climate, 14*, 1479-1498.

Chelton, D. B., M. H. Freilich (2005), Scatterometer-Based Assessment of 10-m Wind Analysis from the Operational ECMWF and NCEP Numerical Weather Prediction Models, *Mon. Wea. Rev., 133*, 409-429.

Clement, A. C., R. Seager, M. A. Cane, S. E, Zebiak (1996), An ocean dynamical thermostat, *J. Climate, 9*, 2190–2196.

Clement, A.C., R. Byrgman J. R. Norris (2009), Observational and Model Evidence for Positive Low-Level Cloud Feedback, *Science, 325*, 460-464.

Cox, M. D. (1980), Generation and propagation of 30-day waves in a numerical model of the Pacific, *J. Phys. Oceanogr., 10,* 1168-1186.

Davey, M., and coauthors, (2002), STOIC: A study of coupled model climatology and variability in tropical ocean regions, *Clim. Dynm., 18*, 403-420.

Delworth, T. L. and coauthors, (2006) GFDL's CM2 global coupled climate models. Part I: Formulation and simulation characteristics, *J. Climate, 19*, 643–674.

Deser, C., J. J. Bates, and S. Wahl (1993), The influence of sea surface temperature gradients on stratiform cloudiness along the equatorial front in the Pacific Ocean, *J. Climate, 6*, 1172–1180.

de Szoeke, S. P., S.-P. Xie (2008), The tropical eastern Pacific seasonal cycle: Assessment of errors and mechanisms in IPCC AR4 coupled ocean-atmosphere general circulation models, *J. Climate, 21*, 2573-2590.

Dewitte, B., C. Cibot, C. Périgaud, S. I. An, and L. Terray (2007), Interaction between near-annual and ENSO modes in a CGCM simulation: Role of equatorial background mean state, *J. Climate, 20*, 1035–1052.

DiNezio, P. N., A. C. Clement, G. A. Vecchi, B. J. Soden, B. P. Kirtman, S. K. Lee (2009), Climate Response of the Equatorial Pacific to Global Warming, *J. Climate, 22*, 4873–4892.

Düing, W., P. Hisard, E. Katz, J. Knauss, J. Meincke, L. Miller, K. Moroshkin, G. Philander, A. Rybnikov, K. Voigt, R. Weisberg (1975), Meanders and long waves in the equatorial Atlantic, *Nature*, *257,* 280-284.

Evans, W., P. G. Strutton, F. P. Chavez (2009), Impact of tropical instability waves on nutrient and chlorophyll distributions in the equatorial Pacific, *Deep-Sea Res.- I., 56*, 178-188.

Fairall, C. W., E. F. Bradley, D. P. Rogers, J. D. Edson, G. S. Young (1996), Bulk parameterization of air-sea fluxes for Tropical Ocean Global Atmosphere Coupled-Ocean Atmosphere Response Experiment, *J. Geophys. Res., 15*, 3747-3764.

Fedorov, A.V., and G. Philander (2001), A stability analysis of the tropical ocean-atmosphere interactions: Bridging Measurements of, and Theory for El Niño, *J. Climate, 14*, 3086-3101.

Flament, P., S. Kennan, R. Knox, P. Niiler, and R. Bernstein (1996), The three-dimensional structure of an upper ocean vortex in the tropical Pacific Ocean, *Nature, 383*, 610- 613.

Giannini, A., R. Saravanan, and P. Chang (2003), Oceanic forcing of Sahel Rainfall on interannual to interdecadal time scales, *Science, 302*, 1027– 1030.

Gorgues, T., C. Menkes, O. Aumont, J. Vialard, Y. Dandonneau, L. Bopp (2005), Biogeochemical impact of tropical instability waves in the equatorial Pacific, *Geophys. Res. Lett., 32*, L24615.

Graham, N. E., T. P. Barnett (1987), Observations of sea surface temperatures, convection and surface wind divergence over tropical oceans, *Science, 238*, 657-659

Haidvogel, D. B., H. G. Arango, K. Hedstrom, A. Beckmann, P. Malanotte-Rizzoli, A. F. Shchepetkin (2000), Model evaluation experiments in the North Atlantic Basin: Simulations in nonlinear terrain-following coordinates, *Dyn. Atmos. Oceans, 32*, 239-281.

Ham, Y. G., I. S. Kang (2010), Improvement of seasonal forecasts with inclusion of tropical instability waves on initial conditions, *Clim. Dymn*., DOI 10.1007/s00382-010-0743-0.

Hansen, D., C. A. Paul (1984), Genesis and effects of long waves in the equatorial Pacific, *J. Geophys. Res.*, *89*, 10431-10440.

Hashizume, H., S.-P. Xie, M. Fujiwara, M. Shiotani, T. Watanabe, Y. Tanimoto, W. T. Liu, K. Takeuchi (2002), Direct Observations of Atmospheric Boundary Layer Response to SST Variations Associated with Tropical Instability Waves over the Eastern Equatorial Pacific, *J. Climate, 15*, 3379–3393.

Hastenrath, S., and L. Greischar, (1993), Further work on the prediction of northeast Brazil rainfall anomalies, *J. Climate, 6*, 743-758,

Hayes, S. P., M. J. McPhaden, J. M. Wallace (1989), The Influence of Sea Surface Temperature on Surface Wind in the Eastern Equatorial Pacific: Weekly to Monthly Variability, J. *Climate, 2*, 1500-1506.

Hazeleger, W., P. de Vries (2003) Fate of the Equatorial Undercurrent in the Atlantic, in Interhemispheric Water Exchange in the Atlantic Ocean, edited by G. J. Goni and P. Malanotte-Rizzoli, pp. 175–191, Elsevier Oceanographic Series.

Hormann, V., and P. Brandt (2007), Atlantic Equatorial Undercurrent and associated cold tongue variability, *J. Geophys. Res., 112*, C06017, doi:10.1029/2006JC003931.

Huffman, G. J., R. F. Adler, D. T. Bolvin, G. Gu, E. J. Nelkin, K. P. Bowman, Y. Hong, E. F. Stocker, D. B. Wolff (2007), The TRMM Multi-satellite Precipitation Analysis: Quasi-Global, Multi-Year, Combined-Sensor Precipitation Estimates at Fine Scale, *J. Hydrometeor., 8*, 38-55.

Jochum, M., P. Malanotte-Rizzoli, A. Busalacchi (2004a), Tropical Instability Waves in the Atlantic Ocean, *Ocean. Modell., 7*, 145-163.

Jochum, M., R. Murtugudde, P. Malanotte-Rizzoli, A. Busalacchi (2004b), Internal variability in the Atlantic Ocean, in Earth Climate: The Ocean-Atmosphere Interaction, Geophys. Monogr. Ser., vol. 147, edited by C. Wang, S.-P. Xie, and J. A. Carton, pp. 181 – 188, AGU, Washington, D. C.

Jochum, M., R. Murtugudde, R. Ferrari, P. Malanotte-Rizzoli (2005), The Impact of Horizontal Resolution on the Tropical Heat Budget in an Atlantic Ocean Model, *J. Climate, 18*, 841–851.

Jochum. M., R. Murtugudde (2006), Temperature Advection by Tropical Instability Waves, *J. Phys. Oceanogr., 36*, 592-605.

Jochum, M., M. F. Cronin, W. S. Kessler, D. Shea (2007), Observed temperature advection by Tropical Instability Waves. *Geophys, Res. Lett., 34*, L09604.

Jochum. M., G. Danabasoglu, M. Holland, Y. O. Kwon, W. G. Large (2008), Ocean viscosity and climate, *J. Geophys. Res., 113*, C06017, doi:10.1029/2007JC004515.

Juang, H. M. H., M. Kanamitsu (1994), The NMC nested regional spectral model, *Mon. Wea. Rev., 122*, 3-26.

Kanamitsu, M., W. Ebisuzaki, J. Woollen, S. K. Yang, J. J. Hnilo, M. Fiorino, G. L. Potter (2002), NCEP-DOE AMIP-II Reanalysis (R-2), *Bull. Am. Meteor. Soc., 83*, 1631-1643.

Kawase, H., T. Yoshikane, M. Hara, F. Kimura, T. Yasunari, B. Ailikun, H. Ueda, and T. Inoue (2009), Intermodel variability of future changes in the Baiu rainband estimated by the pseudo global warming downscaling method, *J. Geophys. Res., 114*, D24110, doi:10.1029/2009JD011803.

Kennan, S. C., P. J. Flament (2000), Observations of a Tropical Instability Vortex, *J. Phys. Oceanogr., 30*, 2277–2301.

Kimura, F., and A. Kitoh (2007), Downscaling by pseudo global warming method, Final Rep., pp.43 – 46, ICCAP, *Res. Inst. for Humanity and Nat*., Kyoto, Japan.

Knutson, T. R., S. Manabe (1995), Time-Mean Response over the Tropical Pacific to Increased CO_2 in a Coupled Ocean-Atmosphere Model, *J. Climate, 8*, 2181–2199.

Knutson, T. R., J. J. Sirutis, S. T. Garner, G. A. Vecchi, and I. M. Held (2008), Simulated reduction in Atlantic hurricane frequency under twenty-first-century warming conditions, *Nat. Geosci., 1*, 359 – 364, doi:10.1038/ngeo202.

Klein, S. A., D. L. Hartmann (1993), The seasonal cycle of low stratiform clouds, *J. Climate, 6*, 1587–1606.

Kug, J.-S., Y.-G. Ham, F.-F. Jin, and I.-S. Kang (2010), Scale interaction between tropical instability waves and low-frequency oceanic flows, Geophys. Res. Lett., 37, L02710, doi:10.1029/2009GL041020.

Legeckis, R. (1977) Long waves in the Eastern Equatorial Pacific Ocean: A View from a Geostationary Satellite, *Science, 197*, 1177-1181.

Legeckis, R., W. Pichel, G. Nesterczuk (1983), Equatorial Long Waves in Geostationary Satellite Observations and in a Multichannel Sea Surface Temperature Analysis, *Bull. Am. Meteorol. Soc., 64*, 133-139.

Löptien, U., C. Eden, A. Timmermann, H. Dietze (2009), Effects of biologically induced differential heating in an eddy-permitting coupled ocean-ecosystem model, *J. Geophys. Res., 114*, C06011.

Li T, Hogan TF, Chang CP (2000) Dynamic and Thermodynamic Regulation of Ocean Warming, *J. Atmos. Sci., 57*, 3353–3365.

Lien, R. C., E. A. D'Asaro, C. E. Menkes (2008), Modulation of equatorial turbulence by tropical instability waves, *Geophys. Res. Lett., 35*, L24607, doi:10.1029/2008GL035860.

Lindzen, R. S., S. Nigam (1987), On the role of sea surface temperature gradients in forcing low-level winds and convergence in the tropics, *J. Atmos. Sci., 44*, 2418 – 2436.

Liu, W. T., X. Xie, P. S. Polito, S.-P. Xie, H. Hashizume (2000), Atmospheric manifestation of tropical instability waves observed by QuikSCAT and Tropical Rain Measuring Mission, *Geophys. Res. Lett., 27*, 2545–2548.

Liu, Z. (1998), The Role of Ocean in the Response of Tropical Climatology to Global Warming: The West-East Contrast, *J. Climate, 11*, 864-875.

Liu. Z., S. Vavrus, F. He, N. Wen, Y. Zhong (2005), Rethinking Tropical Ocean Response to Global Warming: The Enhanced Equatorial Warming, *J. Climate, 18*, 4684–4700.

Masina, S., S. Philander, A. Bush (1999), An analysis of tropical instability waves in a numerical model of the Pacific Ocean-2. Generation and energetics of the waves, J. *Geophys. Res., 104*, 29613-29635.

Mechoso, C., and coauthors (1995), The seasonal cycle over the tropical Pacific in general circulation model, *Mon. Wea. Rev., 123*, 2825-2838.

Meehl. G. A., W. M. Washington (1996), El Niño-like climate change in a model with increased atmospheric CO2 concentration, *Nature, 382*, 56-60.

Menkes, C. E., J. G. Vialard, S. C. Kennan, J. P. Boulanger, G. V. Madec (2006), A modeling of the impact of tropical instability waves on the heat budget of the eastern equatorial Pacific, *J. Phys. Oceanogr, 36*, 847–865.

Miller, R. (1997), Tropical thermostats and low cloud cover, *J. Climate, 10*, 409-440.

Mitchell, T. P., J. M. Wallace (1992), The annual cycle in equatorial convection and sea surface temperature, *J. Climate, 5*, 1140-1156.

Moum, J. N., A. Lien, A. Perlin, J. D. Nash, M. C. Gregg, P. J. Wiles (2009), Sea surface cooling at the Equator by subsurface mixing in tropical instability waves, *Nature Geoscience, 2*, 761-765.

Moura, A. D., J. Shukla (1981), On the dynamics of droughts in northeast Brazil: Observation, theory, and numerical experiments with a general circulation model, *J. Atmos. Sci., 38,* 2653–2675.

Nagura, M., K. Ando, K. Mizuno (2008), Pausing of the ENSO Cycle: A Case Study from 1998 to 2002, J. *Climate, 21*, 342–363.

Okumura, Y., S.-P. Xie (2001), Numaguti A, Tanimoto Y, Tropical Atlantic air-sea interaction and its influence on the NAO, *Geophys. Res. Lett., 28*, 1507-1510.

Philander, S. G. H. (1976), Instabilities of zonal equatorial currents, *J. Geophys. Res., 81*, 3725-3735.

Philander, S. G. H., P. Delecluse (1983), Coastal currents in low latitudes (with application to the Somali and El Niño currents), *Deep-Sea Res., 30*, 887-902.

Qiao, L., R. H. Weisberg (1995), Tropical Instability Wave Kinematics: Observations from the Tropical Instability Wave Experiment (TIWE), *J. Phys. Oceanogr.*, *100*, 8677-8693.

Ramanathan, V., W. Collins (1991), Thermodynamic regulation of ocean warming by cirrus clouds deduced from observations of the 1987 El Niño, *Nature, 351*, 27–32.

Reynolds, R. W., T. M. Smith, C. Liu, D. B. Chelton, K. S. Casey, M. G. Schlax (2007), Daily High-resolution Blended Analyses for sea surface temperature, *J. Climate*, *20*, 5473-5496.

Richter, I., S.-P. Xie (2008), On the origin of equatorial Atlantic biases in coupled general circulation models, *Clim. Dyn., 31*, 587-598.

Roberts, M.J., and co-authors (2009), Impact of resolution on the tropical Pacific circulation in a matrix of coupled models, *J. Climate*, *22*, 2541- 2556.

Ruiz-Barradas, A., J. A. Carton, and S. Nigam (2003), Role of the atmosphere in climate variability of the tropical Atlantic, *J. Climate*, *16*, 2052-2065.

Saravanan R, P. Chang (2000), Interaction between tropical Atlantic variability and El Niño-Southern Oscillation, *J. Climate*, *13*, 2177-2194.

Schott, F. A., M. Dengler, P. Brandt, K. Affler, J. Fischer, B. Bourles, Y. Gouriou, R. L. Molinari, and M. Rhein (2003), The zonal currents and transports at 35°W in the tropical Atlantic, *Geophys. Res. Lett.*, *30*(7), 1349, doi:10.1029/2002GL016849.

Schudlich, R., J. F. Price (1992), Diurnal cycles or current, temperature and turbulent dissipation in a model of the equatorial upper ocean, *J. Geophys. Res., 97*, 5409–5422.

Seager, R., R. Murtugudde (1997), Ocean dynamics, thermocline adjustment, and regulation of tropical SST, *J. Climate, 10*, 521-534.

Seo, H., M. Jochum, R. Murtugudde, A. J. Miller (2006), Effect of Ocean Mesoscale Variability on the Mean State of Tropical Atlantic Climate, *Geophys. Res. Lett., 33*, L09606.

Seo, H., A. J. Miller, J. O. Roads (2007a), The Scripps Coupled Ocean-Atmosphere Regional (SCOAR) model, with applications in the eastern Pacific sector, *J. Climate, 20*, 381-402.

Seo, H., M. Jochum, R. Murtugudde, A.J. Miller and J.O. Roads (2007b), Feedback of Tropical Instability Wave - induced Atmospheric Variability onto the Ocean. *J. Climate, 20*, 5842-5855.

Seo, H, M. Jochum, R. Murtugudde, A. J. Miller, J. O. Roads (2008), Precipitation from African Easterly Waves in a Coupled Model of the Tropical Atlantic, *J. Climate, 21*, 1417-1431.

Shaffrey, L., and coauthors (2009), U.K. HiGEM: The new U.K. high resolution global environment model—Model description and basic evaluation, J. *Climate, 22*, 1861–1896.

Shchepetkin, A. F. , J. C. McWilliams (2005), The regional oceanic modeling system (ROMS): A split-explicit, free-surface, topography-following-coordinate ocean model, *Ocean Modell., 9*, 347–404.

Small, R. J., S. P. de Szoeke, S.-P. Xie, L. O'Neill, H. Seo, Q. Song, P. Cornillon, M. Spall M, and S. Minobe (2008), Air-sea interaction over ocean fronts and eddies, *Dyn. Atmos. Oceans, 45*, 274-319.

Small, R. J., K. J. Richards, S.-P. Xie, P. Dutrieux, and T. Miyama (2009), Damping of Tropical Instability Waves caused by the action of surface currents on stress, *J. Geophys. Res., 114*, C04009.

Strutton, P.G., J. P. Ryan, F. P. Chavez (2001), Enhanced chlorophyll associated with tropical instability waves in the equatorial Pacific, *Geophys. Res. Lett., 28*, 2005–2008.

Sutton, R.T., W. A. Norton, S. P. Jewson (2001), The North Atlantic Oscillation – What role for the ocean? *Atmos. Sci. Lett., 1*(2), doi:10.1006/asle.2000.0018.

Vasubandhu, M. and M. Kanamitsu, (2004), Anomaly Nesting: A Methodology to Downscale Seasonal Climate Simulations from AGCMs, *J. Climate, 17*, 3249-3262.

Vecchi, G. A., B. J. Soden, A. T. Wittenberg, I. M Held, A. Leetmaa, M. J. Harrison (2006), Weakening of tropical Pacific atmospheric circulation due to anthropogenic forcing, *Nature, 441*, doi:10.1038/nature04744.

Vecchi, G. A., B. J. Soden (2007), Global Warming and the Weakening of the Tropical Circulation, *J. Climate, 20*, 4316-4340.

von Schuckmann, K., P. Brandt, C. Eden (2008), Generation of tropical instability waves in the Atlantic Ocean, *J. Geophys. Res., 113*, C08034. doi:10.1029/2007JC004712.

Wallace, J. M., T. P. Mitchell, and C. Deser (1989), The influence of sea surface temperature on surface wind in the eastern equatorial Pacific: Seasonal and interannual variability, *J. Climate, 2,* 1492–1499.

Wang, W, M. J. McPhaden (1999), The Surface-Layer Heat Balance in the Equatorial Pacific Ocean. Part I: Mean Seasonal Cycle, *J. Phys. Oceanogr., 29,* 1812–1831.

Weisberg, R. H. (1984), Instability waves observed on the equator in the Atlantic Ocean during 1983, *Geophys. Res. Lett., 11*, 753-756.

Weisberg, R.H., T. J. Weingartner (1988), Instability waves in the Equatorial Atlantic Ocean, *J. Phys. Oceanogr., 18,* 1641-1657.

Wittenberg, A. T. (2002), ENSO response to altered climates. Ph.D. thesis, Princeton University, 475 pp.

Wittenberg, A. T., A. Rosati, N. C. Lau, J. J. Ploshay (2006), GFDL's CM2 Global Coupled Climate Models. Part III: Tropical Pacific Climate and ENSO, *J. Climate, 19,* 698–722.

Wu, Q., and K. P. Bowman (2007), Multiyear satellite observations of the atmospheric response to Atlantic tropical instability waves, *J. Geophys. Res., 112,* D19104.

Xie, S.-P. (1994), On the genesis of the equatorial annual cycle., J. Climate, 7, 2008-2013.

Xie, S.-P., J. A. Carton (2004), Tropical Atlantic variability: patterns, mechanisms, and impacts, in "Ocean-Atmosphere Interaction and Climate Variability", edited by C. Wang, S.-P. Xie, and J. A. Carton, AGU Press.

Xie, S.-P., T. Miyama, Y. Wang, H. Xu, S. P. de Szoeke, R. J. Small, K. J. Richards, T. Mochizuki, T. Awaji (2007), A regional ocean-atmosphere model for eastern Pacific climate: Towards reducing tropical biases, *J. Climate*, *20*, 1504–1522.

Xie, S.-P., C. Deser, G. A. Vecchi, J. Ma, H. Teng, A. T. Wittenberg (2010), Global warming pattern formation: Sea surface temperature and rainfall, *J. Climate, 23*, 996-986.

Yoder, J. A., S. G. Ackleson, R. T. Barber, P. Flament, W. M. Balch (1994), A line in the sea, *Nature*, *371*, 689 – 692.

Yoshimura, K., and M. Kanamitsu (2009), Specification of external forcing for regional model integrations, *Mon. Wea. Rev.*, *137*, 1409–1421.

Yu, J.-Y., and W. T. Liu, 2003, A linear relationship between ENSO intensity and tropical instability wave activity in the eastern Pacific Ocean, *Geophys. Res. Lett.*, 30(14), 1735, doi:10.1029/ 2003GL017176.

Yu, L., and R. A. Weller (2007), Objectively analyzed air–sea heat fluxes for the global ice-free oceans (1981–2005), *Bull. Amer. Meteor., Soc., 88*, 527–539.

Yu, Z., K. P. McCreary, J. A. Proehl (1995), Meridional asymmetry and energetics of tropical instability waves, *J. Phys. Oceanogr., 25*, 2997-300.

Yu, Z., P. S. Schopf, J. P. McCreary (1997), On the annual cycle of upper-ocean circulation in the eastern equatorial Pacific, *J. Phys. Oceanogr.*, *27*, 309-324.

Zebiak, S. E. (1993), Air-sea interaction in the equatorial Atlantic region, *J. Climate, 6*, 1567-1586.

Zahn M. and H. von Storch, (2010), Decreased frequency of North Atlantic polar lows associated with future climate warming. Nature, 467, 309-312.

Zhang, R. H., A. J. Busalacchi (2008), Rectified effects of tropical instability wave (TIW)-induced atmospheric wind feedback in the tropical Pacific, *Geophys. Res. Lett., 35*, L05608.

Captions for Table and Figures

Table 1. Summary of the heat budget for annual mean and the cold season (June-August) for CTL and GW-CTL averaged over 1°S-3°N for 1998-2007. Mean vertical heat flux includes vertical temperature advection ($-\overline{wT_z}$) and the residual (R) in equation (2) that represents entrainment.

Figure 1. Evolution of annual mean temperature over the equatorial cold tongue (3°S-3°N, 30°W-10°W) from 1980 to 2007. The black contour denotes the increase of temperature by 0.5°C.

Figure 2. (Left) Annual mean SST (°C, color shade) and the 10 m winds and (right) precipitation (mm day^{-1}, color shade) and the surface net heat flux (N m^{-2}, black contour with interval 20 N m^{-2}) for (top) observations (NOAA OI SST Analysis and NCEP2 10m winds, both from 1998-2007, the precipitation from TRMM 3B43 product (1998-2007) and the OAFlux from 1998-2004), (middle) CM2.1 20C simulation (1996-2000) and (bottom) SCOAR CTL run (1998-2007).

Figure 3. (Top) meridional (bottom) zonal transects of annual mean (1998-2007) zonal current speed (cm s^{-1}) from (left) SODA, (middle) SCOAR, (right) CM2.1. The zonal currents are averaged 30°W-10°W for the top panel and 1°S-1°N for the bottom panel. The Equatorial Undercurrent is shown in red shades that flows eastward at depth of ~75 meters. The South Equatorial Current is separated into northern and southern branches across the equatorial and flows westward near the surface.

Figure 4. Seasonal cycle of equatorial cold tongue (1°S-1°N) of (a) CM2.1 20C, (b) SCOAR CTL, (c) OBS, (d) CM2.1 A1B-20C, and (e) SCOAR GW-CTL. (f) The annual cycles of SST (30°W-10°W, 1°S-1°N) in observations (black), CM2.1 20C (blue solid line with circle), CM2.1 A1B (red solid line with circle), SCOAR CTL (blue dashed line with +), and SCOAR GW (red dashed line with +).

Figure 5. Annual mean changes in (left) SST (°C, color shade) and the 10 m winds and (right) precipitation (mm day^{-1}, color shade) and the surface net heat flux (N m^{-2}, black contour with interval 5 N m^{-2}) for (top) CM2.1 and (bottom) SCOAR. Gray contours in (c) and (d) denote that the differences are statistically significant at 95% based on t-test.

Figure 6. Annual mean changes (GW-CTL) in (left) downward shortwave radiation (SWRAD, W/m^2, CI=5 W/m^2) and (right) total cloud amount (CLOUD, %, CI=2%) from SCOAR. Negative values are shown as dashed contours.

Figure 7. Decomposition of the 10-year annual mean vertical temperature advection (°C month^{-1}) in SCOAR averaged over 3°S-3°N based on monthly climatology. (a) $-\langle w\rangle\langle T_z\rangle$, (b) $-\langle w\rangle T_z^*$, (c) $-w^*\langle T\rangle_z$, and (d) the sum of (b) and (c), $-\left(\langle w\rangle T_z^* + w^*\langle T\rangle_z\right)$. Ocean temperature in CTL run is superimposed in each panel in black contours with contour interval of 1°C. Note the different scales between (a) and (b)-(d).

Figure 8. Annual mean (1998-2007) difference (δ, shade) in zonal currents (cm s^{-1}) from (top) SCOAR and (bottom) CM2.1 averaged over (right) 30°W-10°W (left) 1°S-1°N and. The present-day climatological values are superimposed in black contours in each panel with CI=10 cm s^{-1}.

Figure 9. (a) Barotropic conversion (10^{-6} kg m^{-1} s^{-3}), $-\rho_o \vec{u}' \cdot (\vec{u}' \cdot \vec{\nabla}\vec{U})$ for CTL (solid curve) and GW (dashed curve), averaged for upper 100 m over 30°W-10°W for June-Aug of 10 years. (b) Same as (a) except for baroclinic conversion, $-g\rho' w'$. Calculations based on annual mean show the similar results.

Figure 10. (top) June-August averaged eddy kinetic energy (EKE, cm^2 s^{-2}) defined as EKE= ½ ($u'^2 + v'^2$), where ′ denotes 20-40 day band-pass filtering for (a) CTL and (b) GW from 1998-2007. (middle) As in (top) panel except for the variance of 20-40 day filtered SST. (bottom) Annual cycle of (e) EKE and (f) SST variance as a function of calendar month for CTL (blue) and GW (red).

Figure 11. Zonally averaged (30°W-10°W) annual mean heat budget (°C $month^{-1}$, 1998-2007) as a function of latitude. (a) Solid curves are for CTL and dashed for GW. Upwelling and entrainment (black), atmospheric neat heat flux into the ocean (red), mean horizontal advection of temperature (blue) and three-dimensional eddy temperature advection (magenta). (b) Difference (GW-CTL) for upwelling and entrainment (black), net eddy heat flux (magenta), zonal eddy heat flux (red), meridional eddy heat flux (green), and vertical eddy heat flux (blue). (c) Difference (GW-CTL) for atmospheric heat flux (red), net horizontal advection (blue) with zonal (black) and meridional (magenta) component.

Figure 12. Each component of the annual mean eddy temperature advections (°C $month^{-1}$) in (left) CTL and (right) GW averaged from 1998-2007. (a,e) Zonal, (b,f) meridional, (c,g) vertical, and (d,h) the sum. The contour intervals are 0.2 °C $month^{-1}$.

Figure 13. Snapshots from CTL of SST and surface currents on September 7, 1990 showing (a) full fields, (b) zonally high-pass filtered fields (10° longitudes). (c) High-pass filtered SST (thick solid) and wind speed (thin solid) averaged over EQ-2°N.

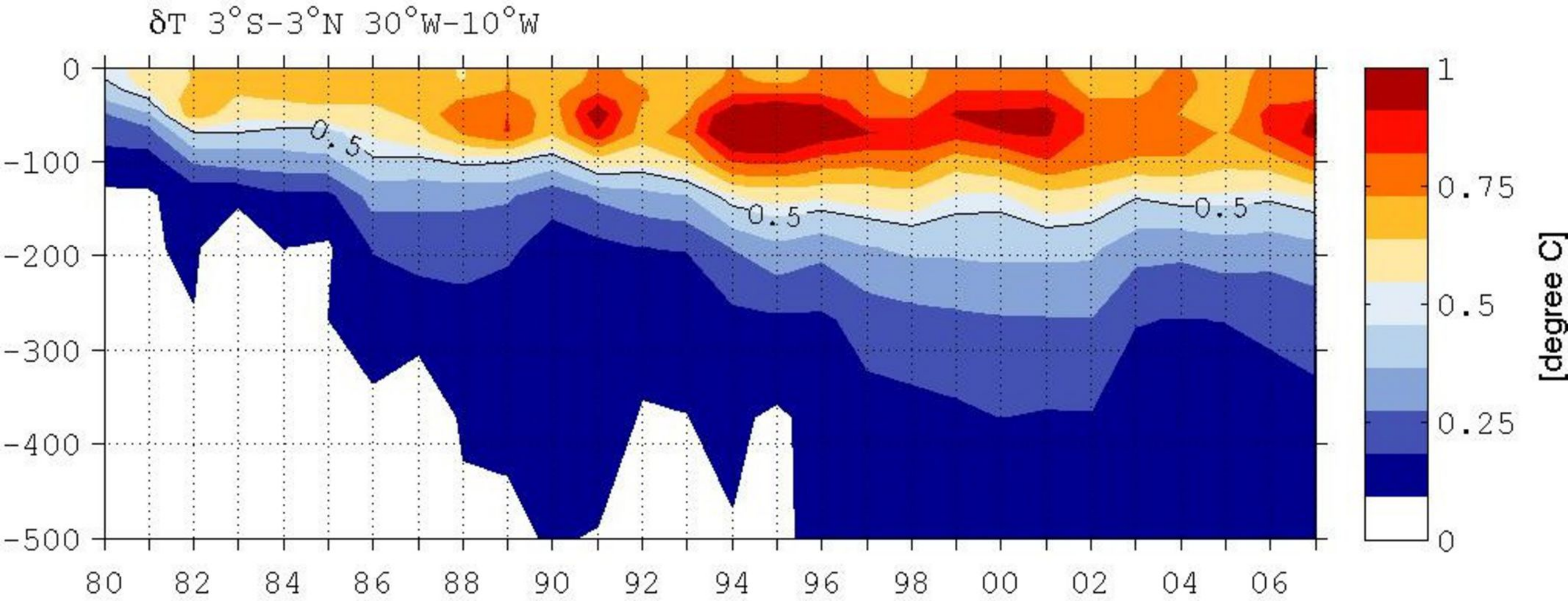
δT 3°S-3°N 30°W-10°W
0
-100
-200
-300
-400
-500
80
82
84
86
88
90
92
94
96
98
00
02
04
06
0.5
0.5
0.5
1
0.75
0.5
0.25
0
[degree C]

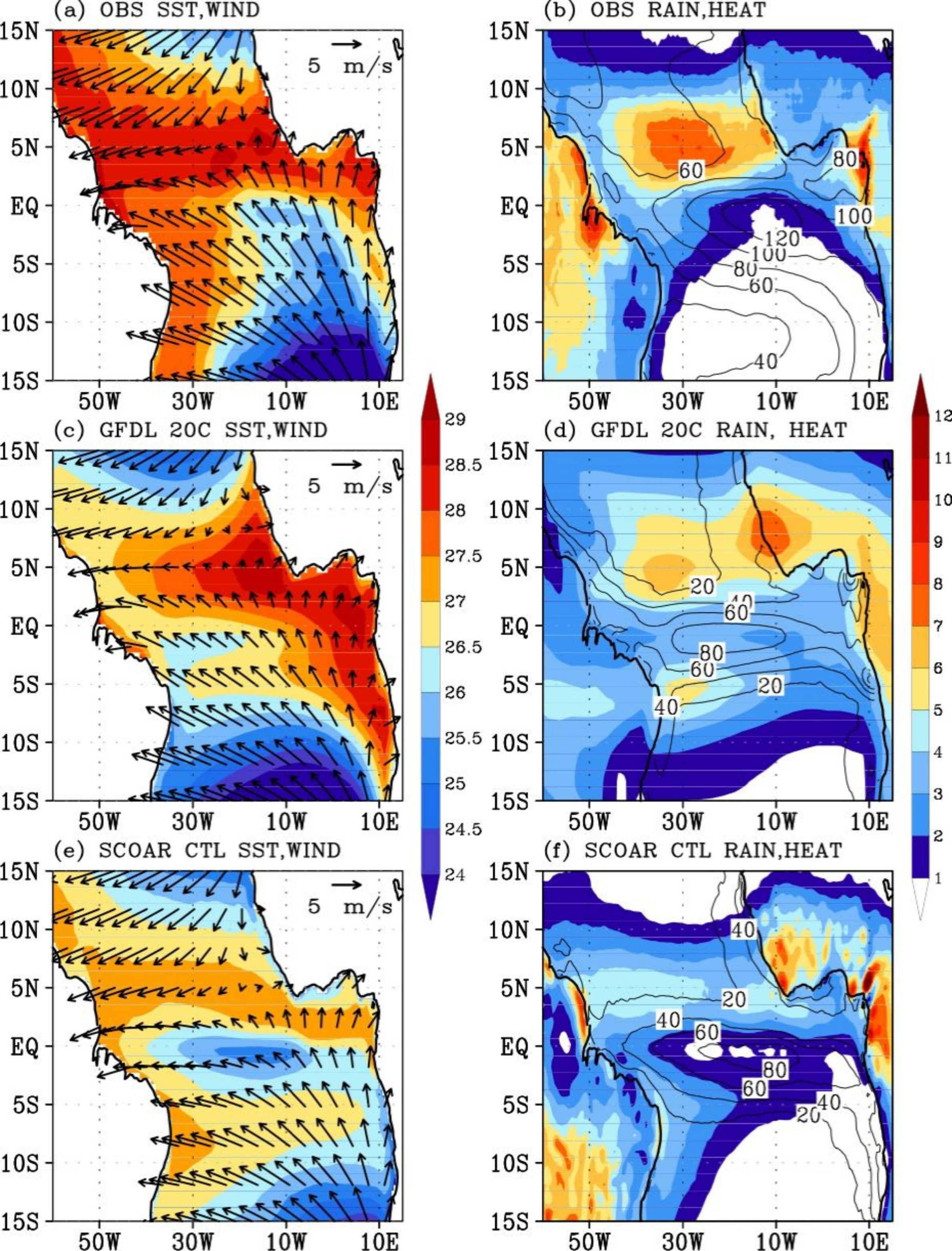

(a) OBS SST,WIND
(b) OBS RAIN,HEAT
(c) GFDL 20C SST,WIND
(d) GFDL 20C RAIN, HEAT
(e) SCOAR CTL SST,WIND
(f) SCOAR CTL RAIN,HEAT
5 m/s
15N
10N
5N
EQ
5S
10S
15S
50W
30W
10W
10E
29
28.5
28
27.5
27
26.5
26
25.5
25
24.5
24
12
11
10
9
8
7
6
5
4
3
2
1
60
80
100
120
40
20

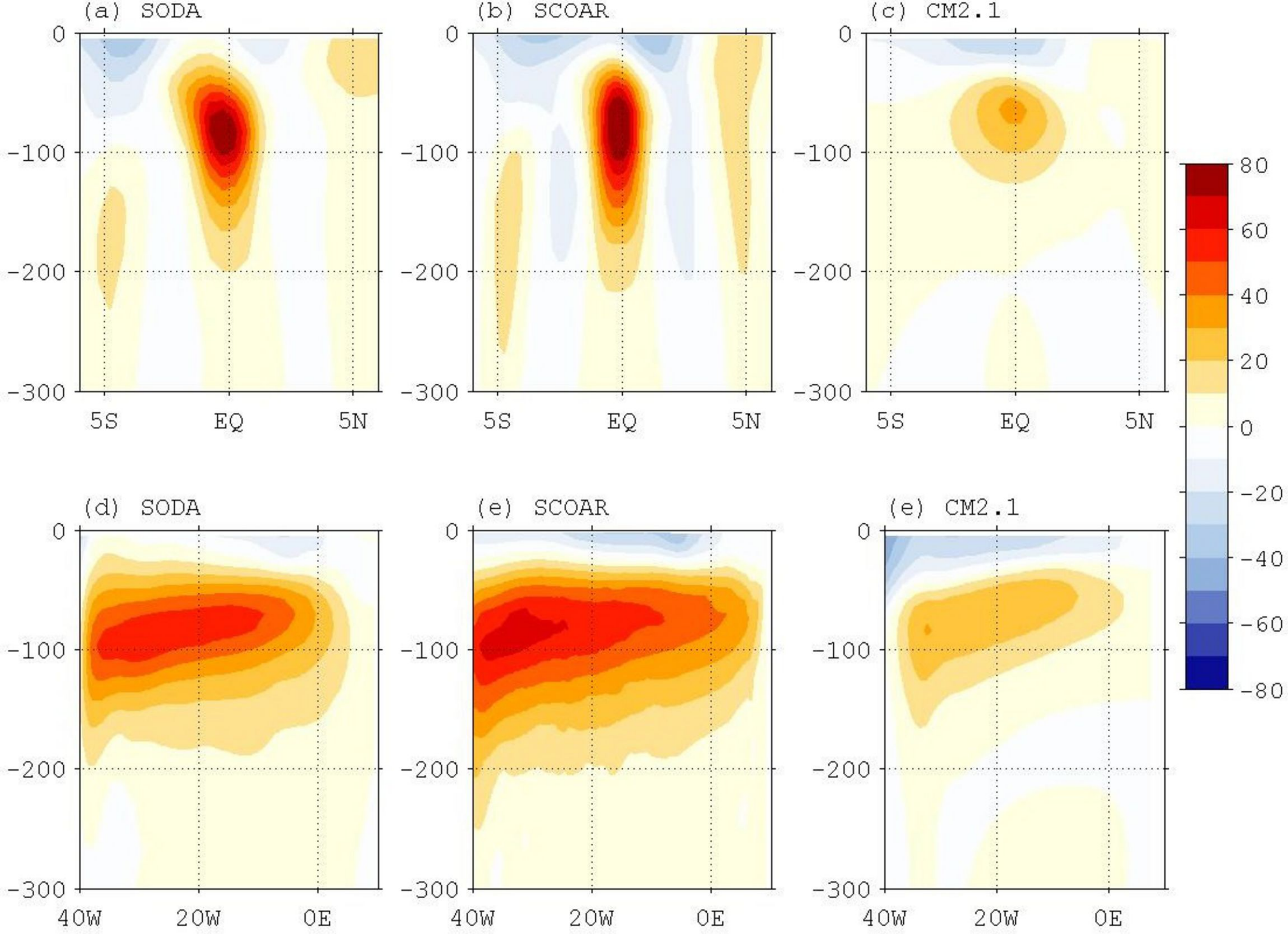
(a) SODA
(b) SCOAR
(c) CM2.1
(d) SODA
(e) SCOAR
(e) CM2.1
0
-100
-200
-300
5S
EQ
5N
40W
20W
0E
80
60
40
20
0
-20
-40
-60
-80

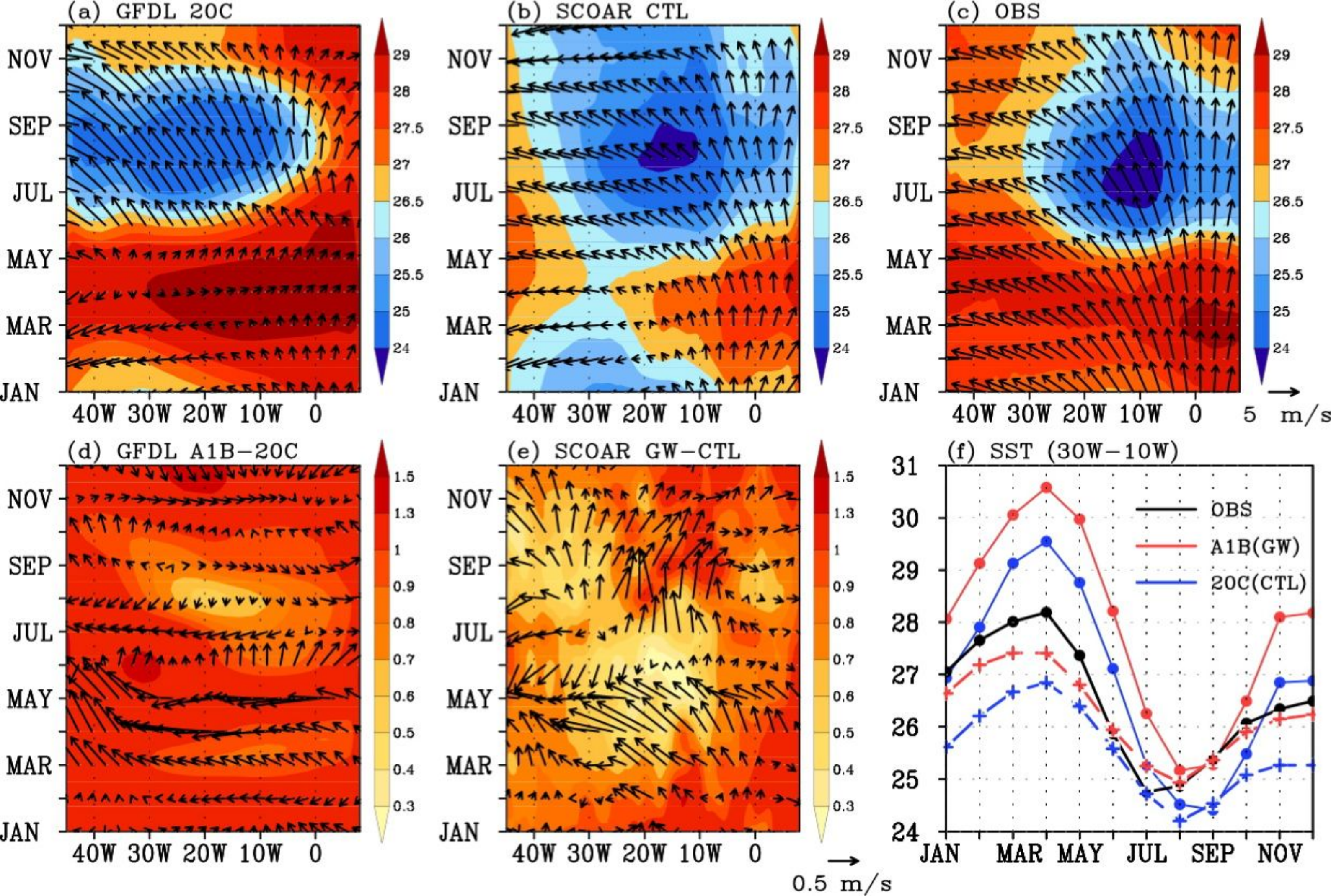

(a) GFDL 20C
(b) SCOAR CTL
(c) OBS
(d) GFDL A1B−20C
(e) SCOAR GW−CTL
(f) SST (30W−10W)
JAN
MAR
MAY
JUL
SEP
NOV
40W 30W 20W 10W 0
29
28
27.5
27
26.5
26
25.5
25
24
1.5
1.3
1
0.9
0.8
0.7
0.6
0.5
0.4
0.3
5 m/s
0.5 m/s
OBS
A1B(GW)
20C(CTL)
31
30
29
28
27
26
25
24

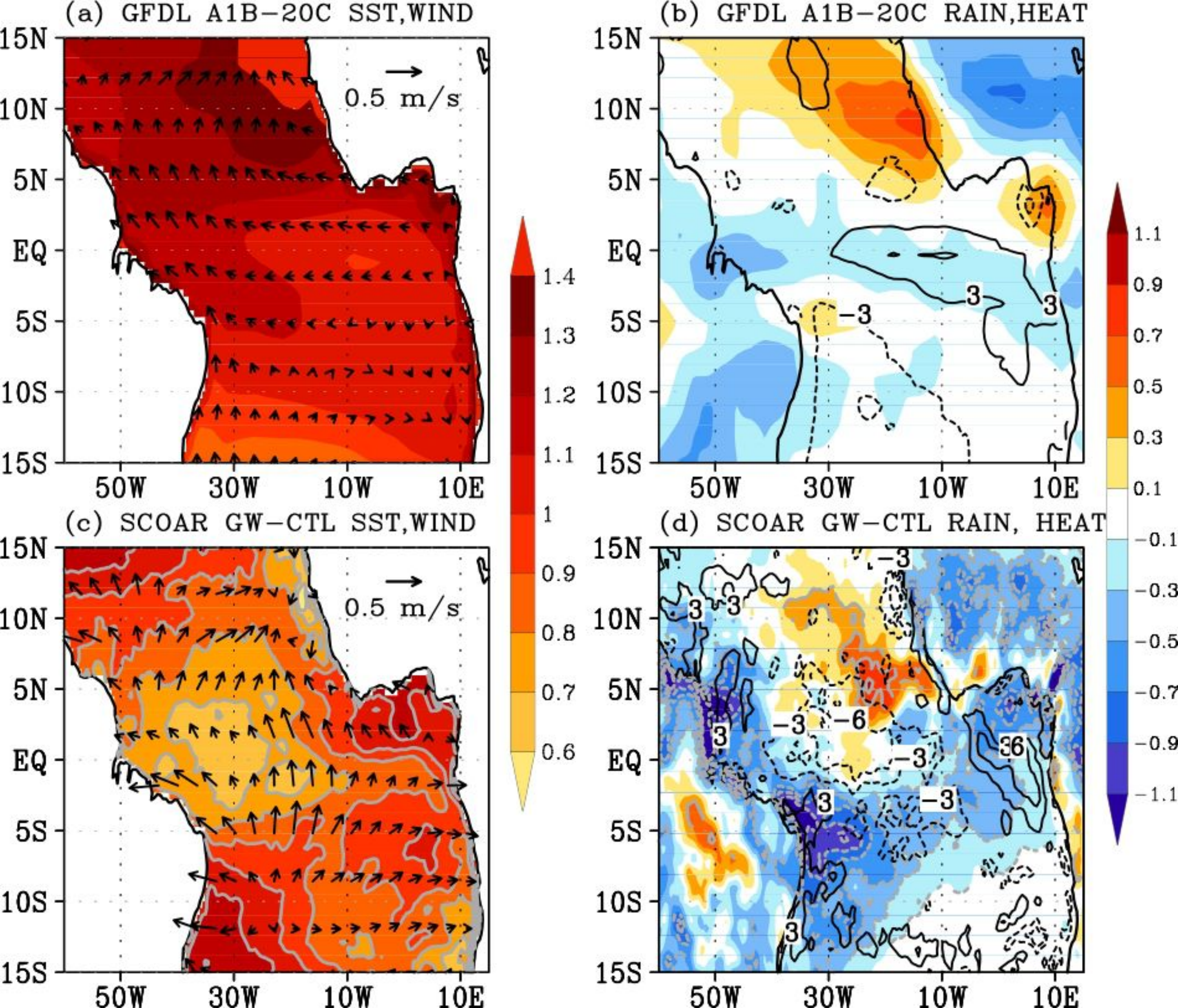

(a) GFDL A1B−20C SST,WIND
(b) GFDL A1B−20C RAIN,HEAT
(c) SCOAR GW−CTL SST,WIND
(d) SCOAR GW−CTL RAIN, HEAT
0.5 m/s
15N
10N
5N
EQ
5S
10S
15S
50W
30W
10W
10E
1.4
1.3
1.2
1.1
1
0.9
0.8
0.7
0.6
1.1
0.9
0.7
0.5
0.3
0.1
−0.1
−0.3
−0.5
−0.7
−0.9
−1.1
3
−3
−6
36

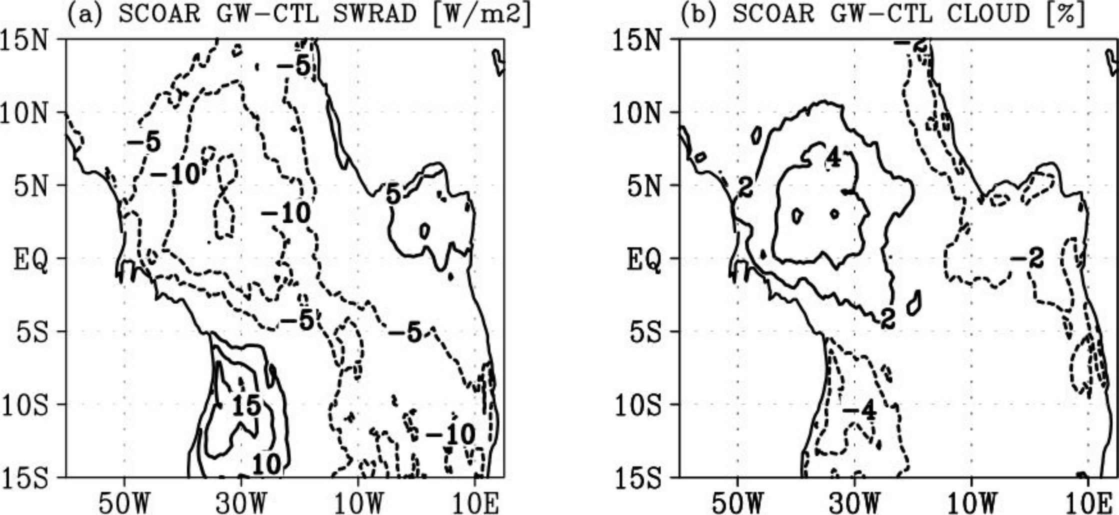
(a) SCOAR GW−CTL SWRAD [W/m2]
(b) SCOAR GW−CTL CLOUD [%]
15N
10N
5N
EQ
5S
10S
15S
50W
30W
10W
10E
−5
−10
5
15
10
2
4
−2
−4

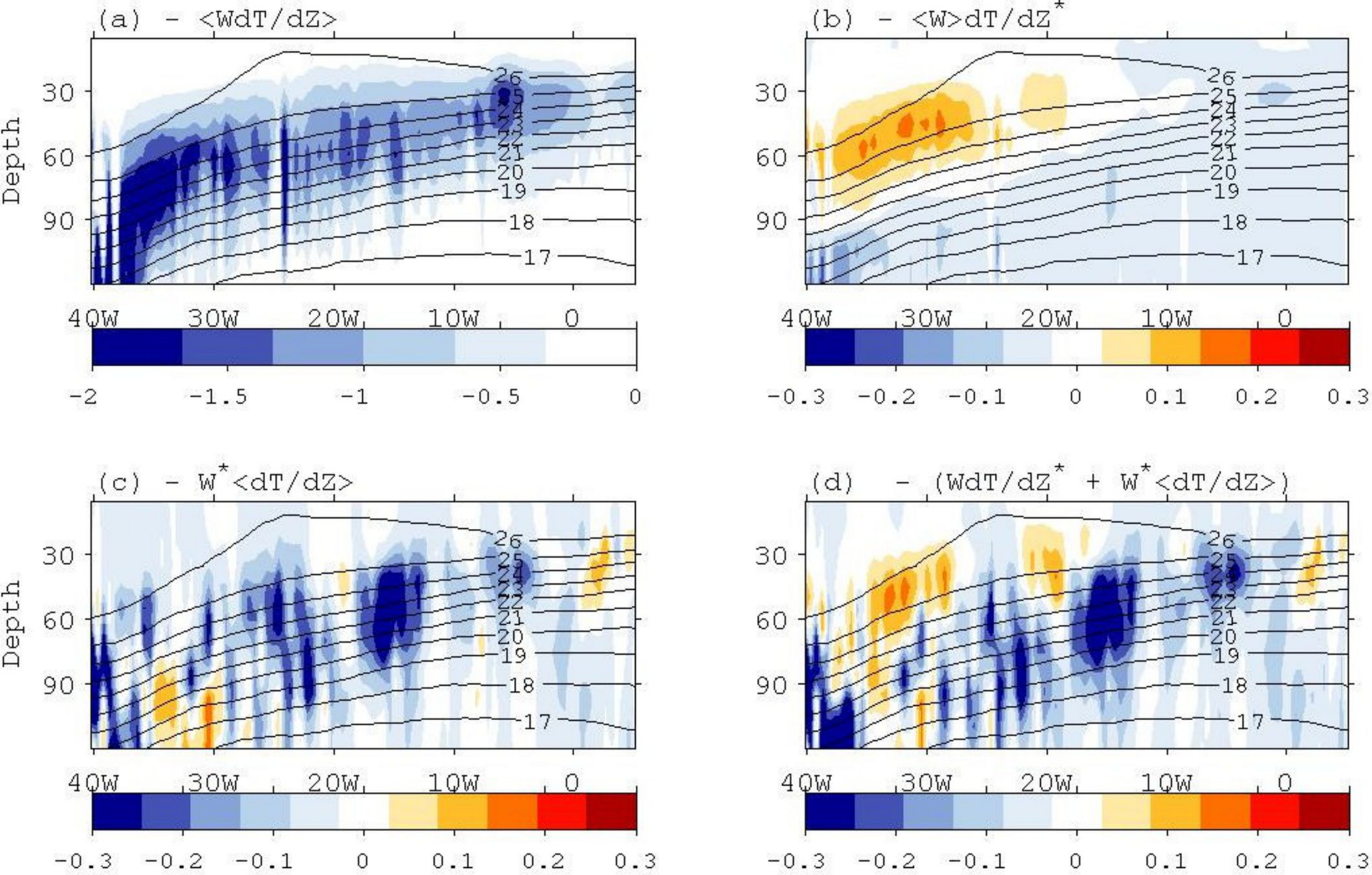
(a) - <WdT/dZ>
(b) - <W>dT/dZ*
(c) - W*<dT/dZ>
(d) - (WdT/dZ* + W*<dT/dZ>)
Depth
30
60
90
40W
30W
20W
10W
0
26
25
24
23
22
21
20
19
18
17
-2
-1.5
-1
-0.5
0
-0.3
-0.2
-0.1
0
0.1
0.2
0.3

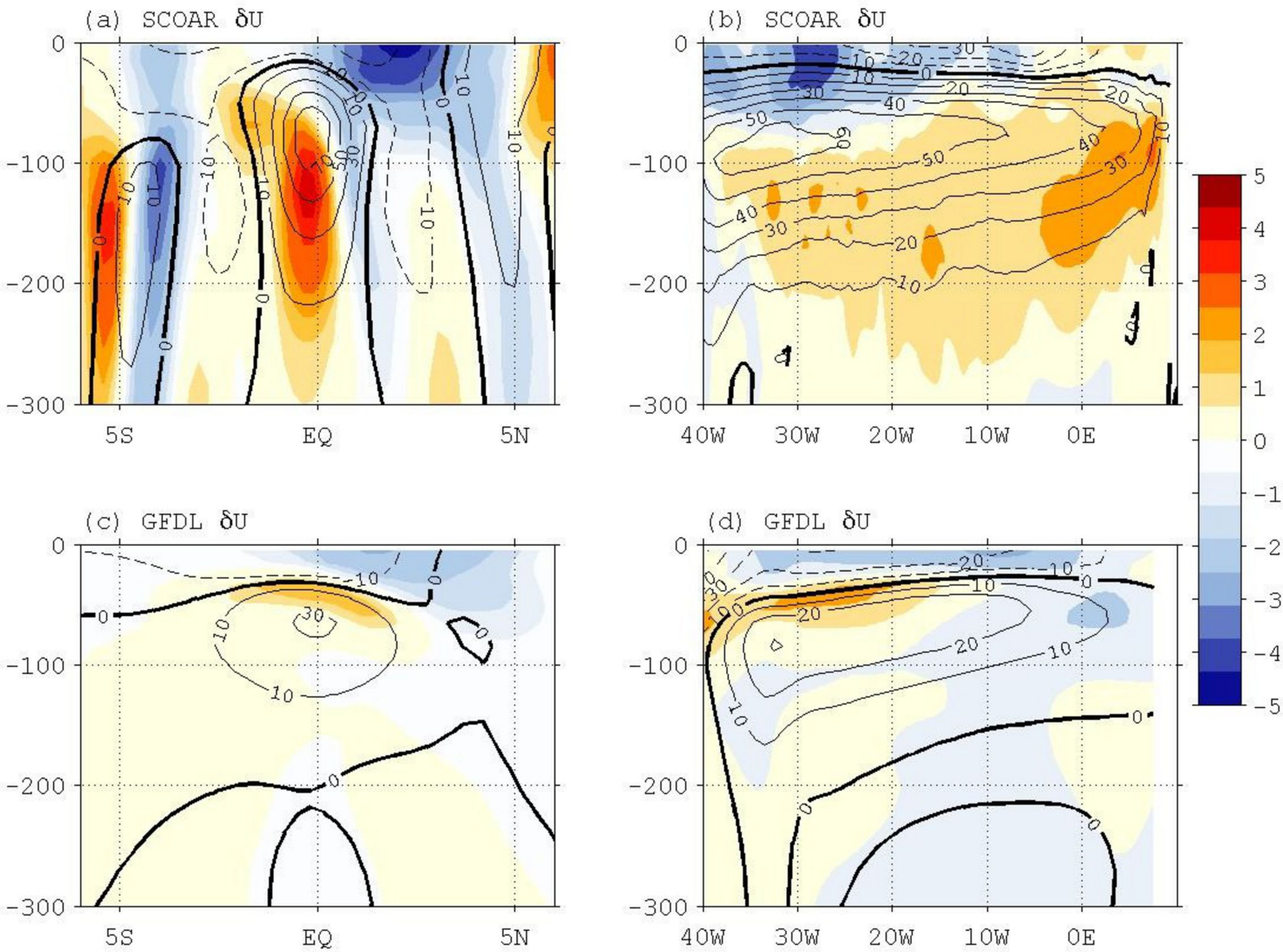

(a) SCOAR δU
(b) SCOAR δU
(c) GFDL δU
(d) GFDL δU
0
-100
-200
-300
5S
EQ
5N
40W
30W
20W
10W
0E
5
4
3
2
1
0
-1
-2
-3
-4
-5

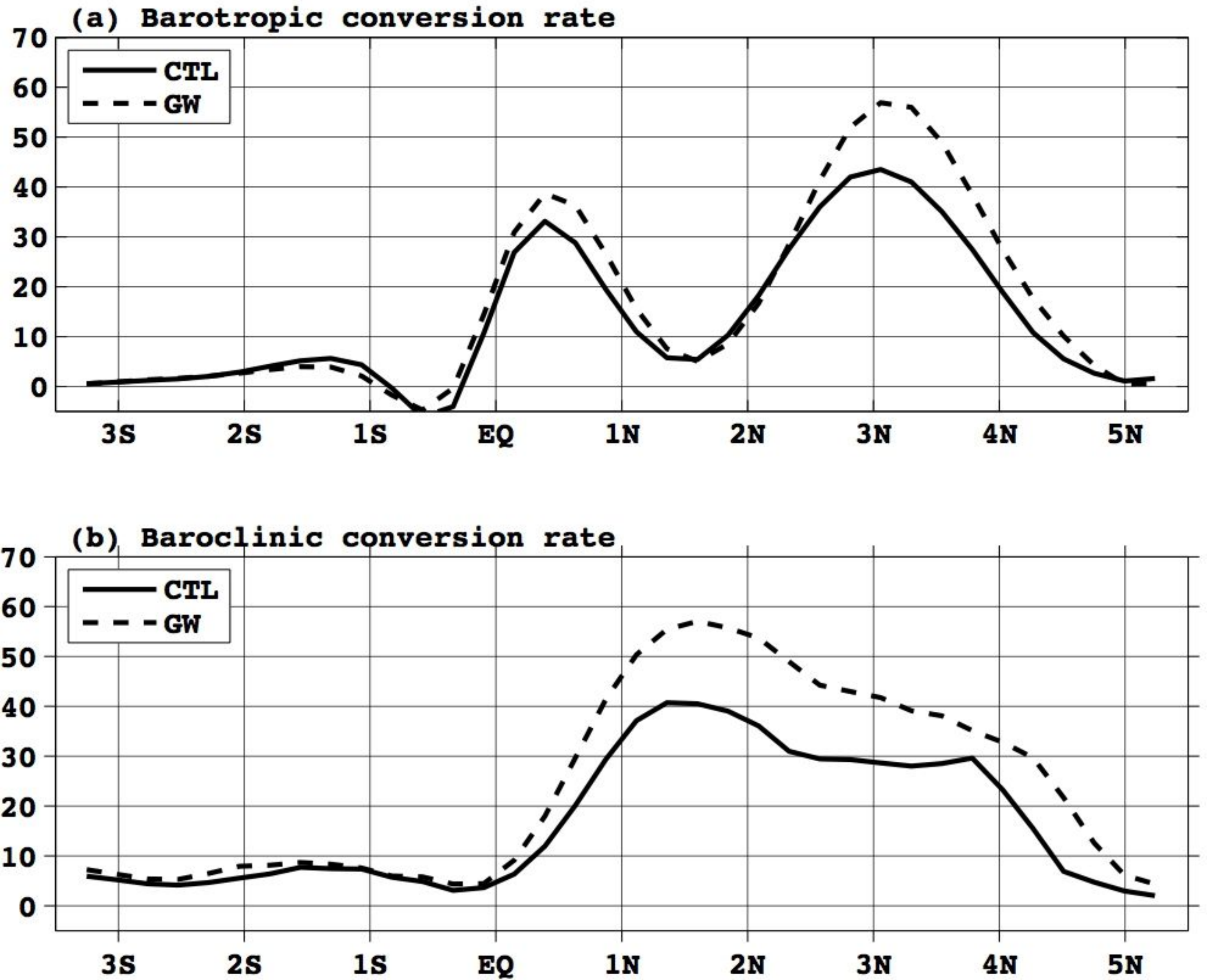

(a) Barotropic conversion rate
CTL
GW
70
60
50
40
30
20
10
0
3S
2S
1S
EQ
1N
2N
3N
4N
5N
(b) Baroclinic conversion rate
CTL
GW
70
60
50
40
30
20
10
0
3S
2S
1S
EQ
1N
2N
3N
4N
5N

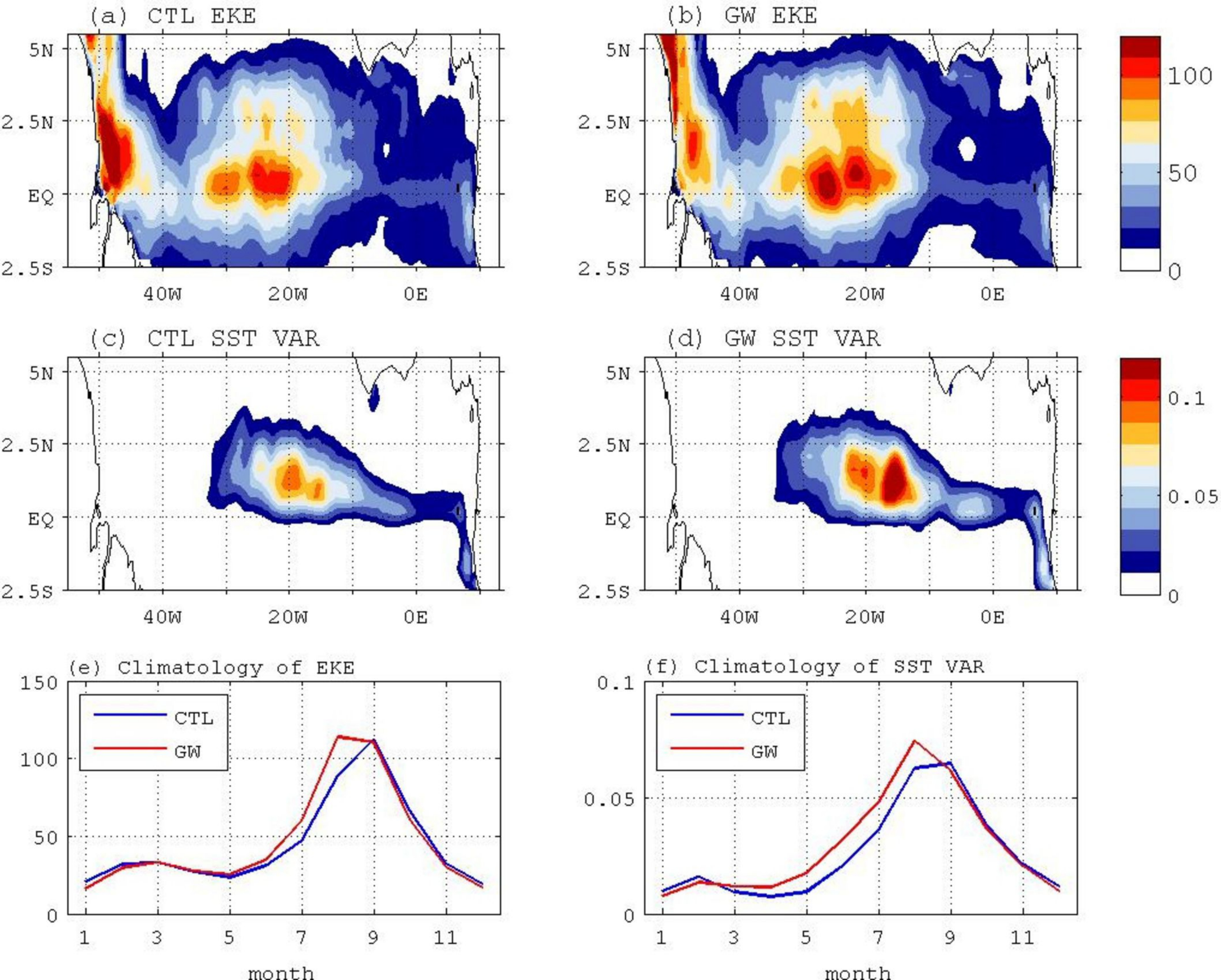

(a) CTL EKE
(b) GW EKE
(c) CTL SST VAR
(d) GW SST VAR
(e) Climatology of EKE
(f) Climatology of SST VAR
5N
2.5N
EQ
2.5S
40W
20W
0E
0
50
100
0.05
0.1
CTL
GW
month
1
3
5
7
9
11
150

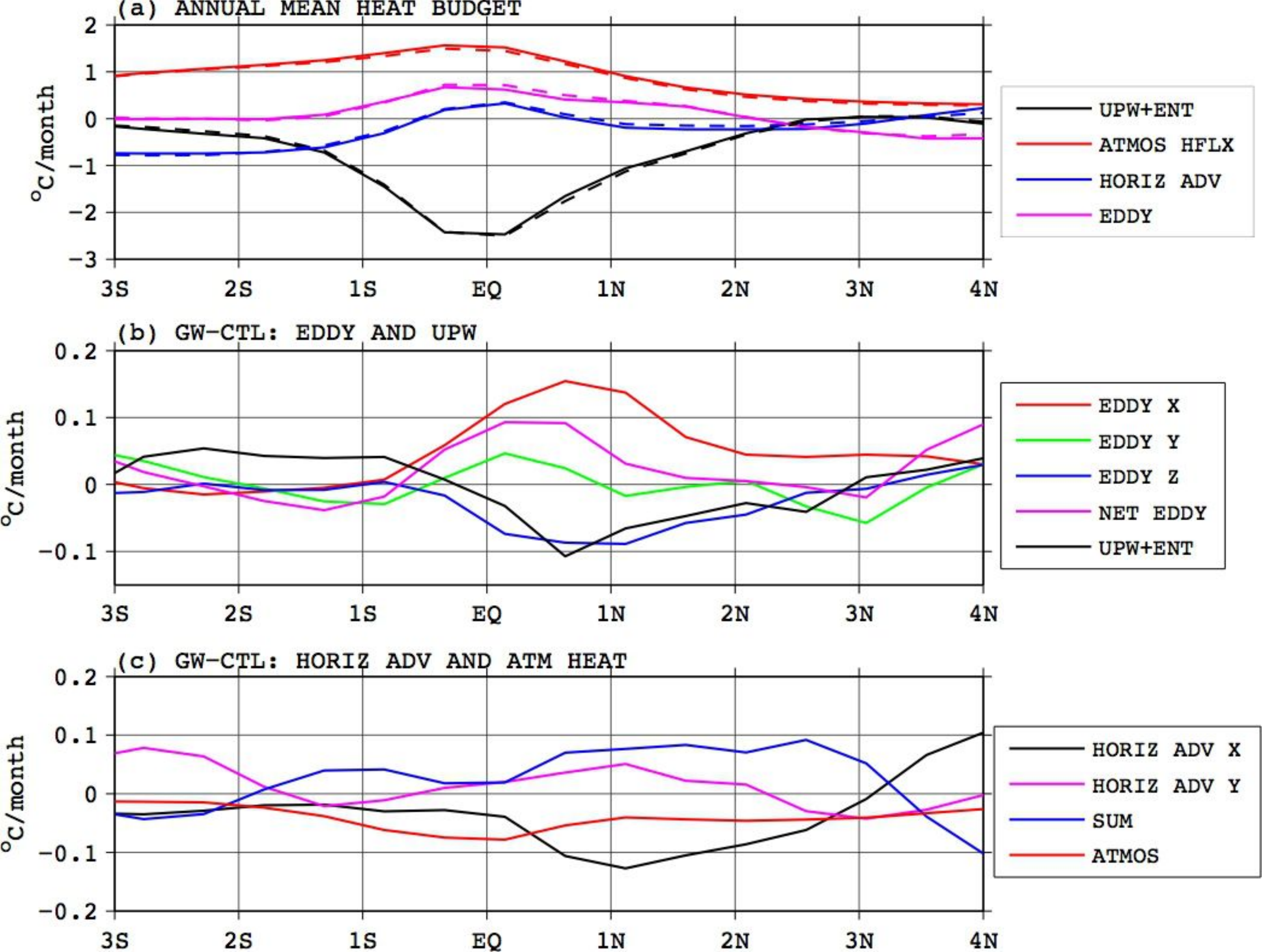

(a) ANNUAL MEAN HEAT BUDGET
°C/month
2
1
0
−1
−2
−3
3S
2S
1S
EQ
1N
2N
3N
4N
UPW+ENT
ATMOS HFLX
HORIZ ADV
EDDY
(b) GW-CTL: EDDY AND UPW
°C/month
0.2
0.1
0
−0.1
EDDY X
EDDY Y
EDDY Z
NET EDDY
UPW+ENT
(c) GW-CTL: HORIZ ADV AND ATM HEAT
°C/month
0.2
0.1
0
−0.1
−0.2
HORIZ ADV X
HORIZ ADV Y
SUM
ATMOS

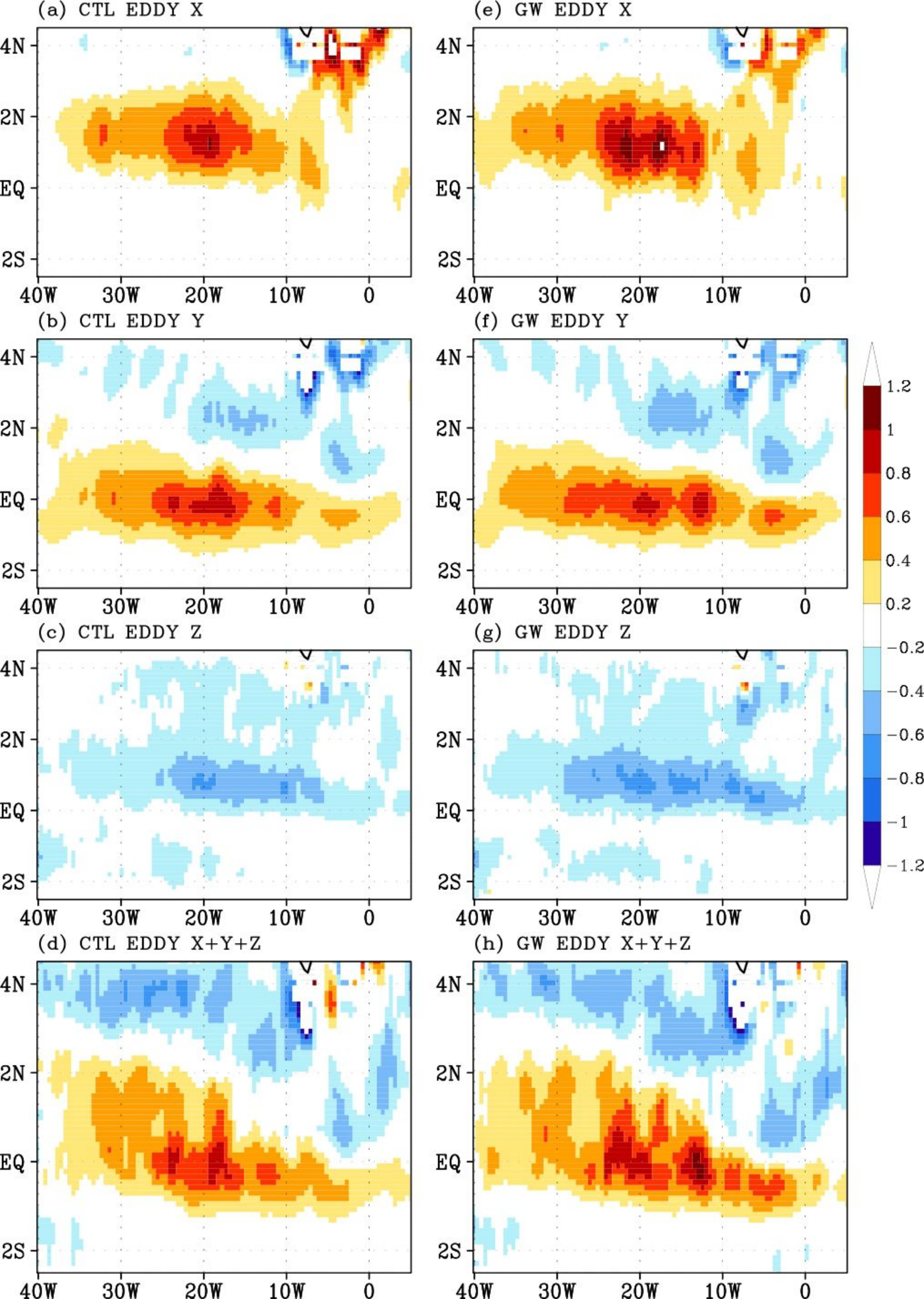

(a) CTL EDDY X
(e) GW EDDY X
(b) CTL EDDY Y
(f) GW EDDY Y
(c) CTL EDDY Z
(g) GW EDDY Z
(d) CTL EDDY X+Y+Z
(h) GW EDDY X+Y+Z
4N
2N
EQ
2S
40W
30W
20W
10W
0
1.2
1
0.8
0.6
0.4
0.2
−0.2
−0.4
−0.6
−0.8
−1
−1.2

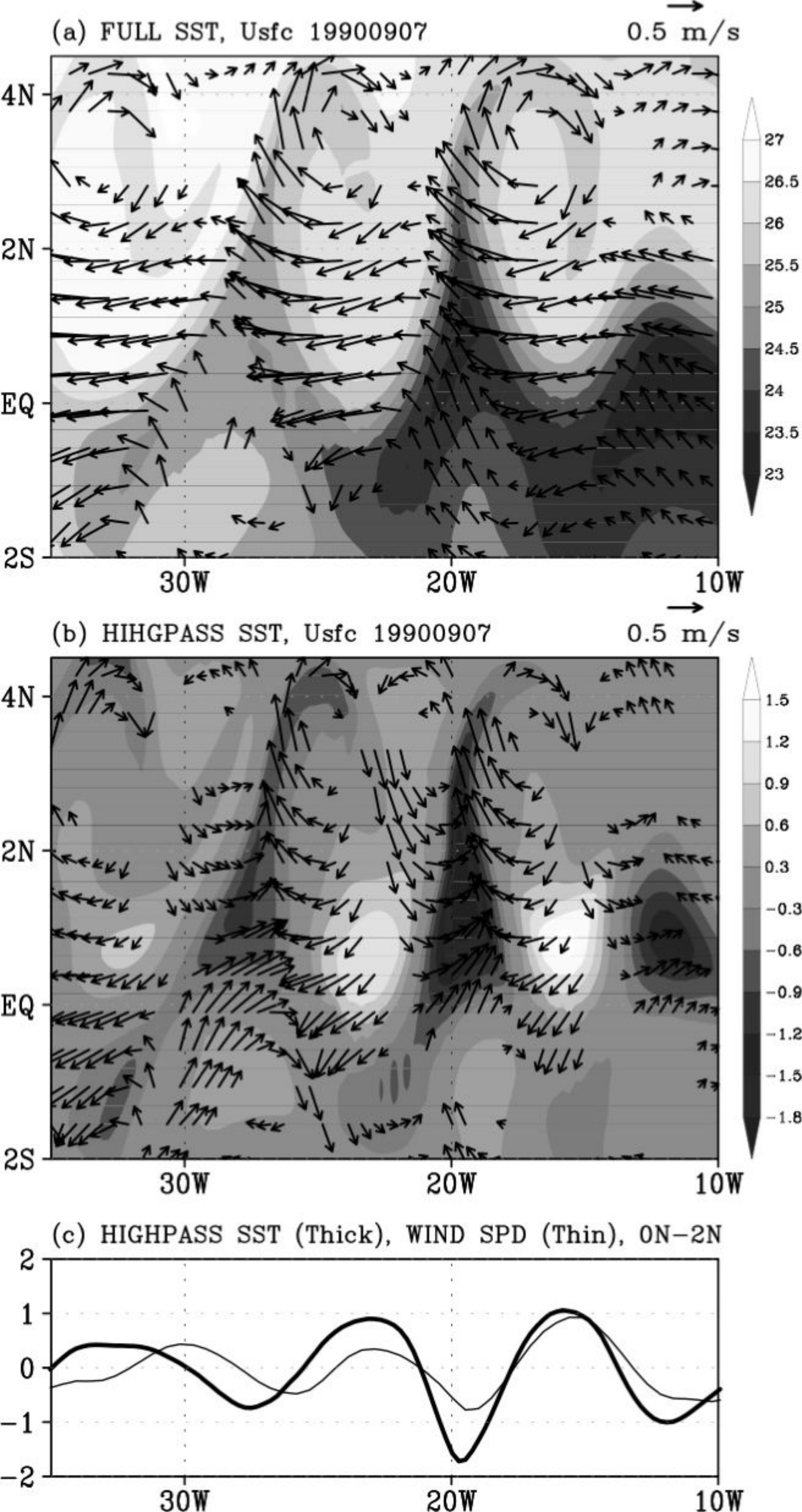

(a) FULL SST, Usfc 19900907
0.5 m/s
4N
2N
EQ
2S
30W
20W
10W
27
26.5
26
25.5
25
24.5
24
23.5
23
(b) HIHGPASS SST, Usfc 19900907
0.5 m/s
4N
2N
EQ
2S
30W
20W
10W
1.5
1.2
0.9
0.6
0.3
−0.3
−0.6
−0.9
−1.2
−1.5
−1.8
(c) HIGHPASS SST (Thick), WIND SPD (Thin), 0N−2N
2
1
0
−1
−2
30W
20W
10W

CTL (GW-CTL)		Annual (°C month^{-1})		JJA (°C month^{-1})	
Net surface heat flux		0.80 (-0.05)		0.22 (-0.15)	
Mean vertical heat flux		-0.91(-0.05)		-0.86 (-0.02)	
Eddy heat flux	$-u'T'_x$	0.15 (0.03)	0.40 (0.08)	0.30 (0.12)	0.46 (0.20)
	$-v'T'_y$		0.06 (0)		0.24 (0)
	$-w'T'_z$		-0.30 (-0.05)		-0.40 (-0.08)
Mean horizontal advection		-0.05 (0.07)		0.06 (0.09)	
Temperature tendency		0 (0)		-0.29 (-0.04)	